SuperFaB: a fabulous code for Spherical Fourier-Bessel decomposition

Henry S. Grasshorn Gebhardt[1, 2, *] and Olivier Doré[1, 2]

[1] *Jet Propulsion Laboratory, California Institute of Technology, Pasadena, CA 91109, USA*
[2] *California Institute of Technology, Pasadena, CA 91125, USA*

The spherical Fourier-Bessel (SFB) decomposition is a natural choice for the radial/angular separation that allows optimal extraction of cosmological information from large volume galaxy surveys. In this paper we develop a SFB power spectrum estimator that allows the measurement of the largest angular and radial modes with the next generation of galaxy surveys. The code measures the pseudo-SFB power spectrum, and takes into account mask, selection function, pixel window, and shot noise. We show that the local average effect is significant only in the largest-scale mode, and we provide an analytical covariance matrix. By imposing boundary conditions at the minimum and maximum radius encompassing the survey volume, the estimator does not suffer from the numerical instabilities that have proven challenging in the past. The estimator is demonstrated on simplified *Roman*-like, *SPHEREx*-like, and *Euclid*-like mask and selection functions. For intuition and validation, we also explore the SFB power spectrum in the Limber approximation. We release the associated public code written in `Julia`.

Keywords: cosmology; large-scale structure

I. INTRODUCTION

One of the aims of future galaxy surveys such as the *Nancy Grace Roman Space Telescope*, *SPHEREx*, *Euclid*, DESI, PFS (Spergel *et al.* 2015, Doré *et al.* 2014, Amendola *et al.* 2018, DESI Collaboration *et al.* 2016, Takada *et al.* 2014) is to answer questions that require measurement of the galaxy overdensity power spectrum on very large cosmological scales. Chiefly among those is the study of modified theories of gravity (e.g. Munshi *et al.* 2016) and the measurement of primordial non-Gaussianity that manifests itself in the power spectrum as a scale-dependent galaxy bias $\propto k^{-2}$ in the simplest models (Salopek and Bond 1990, Komatsu and Spergel 2001, Dalal *et al.* 2008, Desjacques *et al.* 2018). However, the measurement of these large scales is not without challenge.

Large *angular* scales are difficult to exploit fully with a standard 3D power spectrum analysis due to line-of-sight effects such as redshift-space distortions (RSD). When the angular separation between galaxies is large, the assumption that a single line of sight can be used for both galaxies breaks down, which results in a loss of information from the measurement. On medium large scales the problem can be mitigated by choosing a common line of sight for each pair of galaxies (Yamamoto *et al.* 2006, Bianchi *et al.* 2015, Scoccimarro 2015). However, on very large angular scales, the Yamamoto estimator suffers from the same problem as a fixed-LOS estimator. For example, for a full-sky survey, a fixed LOS estimator is expected to measure a vanishing quadrupole. An optimal power spectrum measurement, therefore, needs to allow for a different line of sight for every galaxy in the survey.

Large *radial* scales pose a different kind of challenge, and in the past have mostly been treated by splitting surveys into redshift bins (e.g., Beutler *et al.* 2017). The advantage is that it makes the analysis simple. However, modes larger than the redshift bin are not measured in the radial direction, and that information is lost by such an analysis.

In this paper, we study and implement a method that enables accurate measurements of the largest radial and angular scales mapped by coming surveys. It relies on the spherical Fourier-Bessel (SFB) transform. Most past measurements of the galaxy overdensity power spectrum rely on Fourier decomposition as it decreases the computation cost of near optimal statistical estimators. While a standard Fourier transform decomposes a field into a linear composition of eigenfunctions to the Laplacian in Cartesian coordinates, the SFB transform we consider does the same but in spherical coordinates. Not only does it maintain the statistical and computational advantages of Fourier methods, but it is also the natural coordinate system for the angular/radial separation over the sphere. The radial line of sight for every single galaxy is built into the method, and the modeling of redshift evolution of galaxy bias and growth factor is straightforward. An overview of the SFB power spectrum is given in Pratten and Munshi (2013) and a mathematical treatment clarifying the relation between the configuration-space correlation function, Fourier space correlation function, SFB correlation function, and mixed-space correlation functions can be found in Reimberg *et al.* (2016).

The spherical Fourier-Bessel transform for the analysis of galaxy surveys has been considered multiple times in the past. Binney and Quinn (1991) used a SFB decomposition to characterize overdensities deep in the nonlinear regime. Lahav (1993) applied the SFB analysis to local galaxies on larger scales. Heavens and Taylor (1995) applied the SFB analysis to the IRAS 1.2-Jy galaxy catalogue, Tadros *et al.* (1999) applied it to the PSCz galaxy

* henry.s.gebhardt@jpl.nasa.gov; NASA Postdoctoral Program Fellow

catalogue, and Percival *et al.* (2004) use it in the context of the 2dF Galaxy Redshift Survey. Leistedt *et al.* (2012) have provided a public SFB code, 3DEX, that performs the SFB decomposition first in the radial direction for each galaxy individually, then performs the angular transform using HEALPix. More recently, Wang *et al.* (2020) have built a combined SFB/$P(k)$ estimation code that uses SFB on very large scales, and a Cartesian multipole power spectrum estimator on smaller scales.

SFB power spectrum measurements tended to be plagued by numerical instabilities and computational complexity. The source of the numerical instability is the incomplete coverage of the analysis volume by the survey. For example, typically a boundary condition is applied at some distance $r_{\rm max}$, and the analysis is performed for the entire volume inside a sphere of radius $r_{\rm max}$. However, most surveys will leave most of that volume unexplored, and the de-convolution of the window function or the inversion of the covariance matrix become numerically unstable. The numerical complexity stems from the large number of modes that need to be calculated even when a large fraction of the analysis volume remains empty. Another source of computational complexity is the combined estimation of the real-space power spectrum and redshift-space distortion parameters that requires repeated estimations of the power spectrum (Wang *et al.* 2020).

The spherical Fourier Bessel decomposition code presented in this paper, *SuperFaB*, combines several approaches to address these problems. For the first time, we limit the redshift range by introducing a boundary condition at $r_{\rm min}$ as suggested by Samushia (2019). We also use the 3DEX approach by Leistedt *et al.* (2012) that does not suffer from pixel window effects in the radial direction. The 3DEX approach also allows separation of the angular and radial transforms, and for the angular transform we use HEALPix (Górski *et al.* 2005, Zonca *et al.* 2019). Our bandpower binning is done similar to that for CMB measurements (Hivon *et al.* 2002, Alonso *et al.* 2019).

An alternative to the SFB analysis that also naturally performs the angular/radial separation is spherical harmonic tomography (SHT, see e.g. Camera *et al.* 2018, Nicola *et al.* 2014) where an angular spherical harmonic analysis is performed on shells of redshift bins. Lanusse *et al.* (2015) conclude that SFB yields similar constraints as SHT, but when it comes to marginalizing over systematic biases such as evolving scale-dependent galaxy bias, SFB performs better. Additionally, Castorina and White (2018) developed various approaches to incorporating wide-angle effects in Fourier based estimators. Beutler *et al.* (2019) implement a small-angle expansion for the standard multipole power spectrum.

In section Section II we review the SFB power spectrum and develop intuition in the Limber approximation. Section III details the approach taken for the SFB decomposition, window de-convolution, shot noise, bandpower binning, local average effect, and covariance matrix. We show comparisons with log-normal simulations in Section IV for *Roman*, *SPHEREx*, and *Euclid*, and we conclude in Section V. We leave to the appendices a collection of useful formulae in Appendix A, review the Laplacian in an expanding universe in Appendix B, derive the radial potential boundary conditions in Appendix C, and simplify the covariance matrix in Appendices D and E. Our *SuperFaB* code is publically available at `https://github.com/hsgg/SphericalFourierBesselDecompositions.jl`.

II. SFB POWER SPECTRUM

In this section we develop the SFB formalism. We start with the basic transformation between configuration space and SFB space as well as between Fourier space and SFB space. We then briefly show the power spectrum in a completely homogeneous and isotropic universe before adding in selection function, linear growth factor, galaxy bias, and RSD. We develop intuition by applying Limber's approximation.

The spherical Fourier-Bessel decomposition expresses a field $\delta(\boldsymbol{r})$ in terms of eigenfunctions of the Laplacian in spherical coordinates. For more details, we refer the reader to Section III A. We define the spherical Fourier-Bessel modes $\delta_{\ell m}(k)$ by

$$\delta(\boldsymbol{r}) = \int \mathrm{d}k \sum_{\ell m} \left[\sqrt{\frac{2}{\pi}}\, k\, j_\ell(kr)\, Y_{\ell m}(\theta,\phi)\right] \delta_{\ell m}(k)\,, \quad (1)$$

$$\delta_{\ell m}(k) = \int \mathrm{d}^3\boldsymbol{r} \left[\sqrt{\frac{2}{\pi}}\, k\, j_\ell(kr)\, Y^*_{\ell m}(\hat{\boldsymbol{r}})\right] \delta(\boldsymbol{r})\,, \quad (2)$$

where $\boldsymbol{r} = r\hat{\boldsymbol{r}}$ is the position vector, r is the comoving angular diameter distance from the origin, and $\hat{\boldsymbol{r}}$ is the direction on the sky. The orthogonality relations Eqs. (A6) and (A7) for the spherical Bessel functions and spherical harmonics are used to prove that Eqs. (1) and (2) are inverses of each other. The factor $2k^2/\pi$ can be split between Eqs. (1) and (2) as pleased. Here we use the convention in Nicola *et al.* (2014), because for a non-evolving, homogeneous, and isotropic universe the SFB power spectrum then equals $P(k)$, see Eq. (7) below.

The relation between the SFB coefficients $\delta_{\ell m}(k)$ and the Fourier modes $\delta(\boldsymbol{k})$ is obtained by expressing $\delta(\boldsymbol{r})$ in terms of its Fourier transform in Eq. (2),

$$\delta_{\ell m}(k) = \sqrt{\frac{2}{\pi}}\, k \int \mathrm{d}^3 r\, j_\ell(kr)\, Y^*_{\ell m}(\hat{\boldsymbol{r}}) \int \frac{\mathrm{d}^3 q}{(2\pi)^3}\, e^{i\boldsymbol{q}\cdot\boldsymbol{r}}\, \delta(\boldsymbol{q})\,. \quad (3)$$

With Rayleigh's formula Eq. (A10) this turns into

$$\begin{aligned}\delta_{\ell m}(k) &= \int \frac{\mathrm{d}^3 q}{(2\pi)^3} \sqrt{\frac{\pi}{2q^2}}\, 4\pi \sum_{\ell' m'} i^{\ell'}\, Y^*_{\ell' m'}(\hat{\boldsymbol{q}})\, \delta(\boldsymbol{q}) \\ &\quad \times \frac{2kq}{\pi} \int \mathrm{d}r\, r^2\, j_\ell(kr)\, j_{\ell'}(qr) \\ &\quad \times \int \mathrm{d}^2\hat{\boldsymbol{r}}\, Y^*_{\ell m}(\hat{\boldsymbol{r}})\, Y_{\ell' m'}(\hat{\boldsymbol{r}}) \\ &= \frac{k}{(2\pi)^{\frac{3}{2}}}\, i^\ell \int \mathrm{d}^2\hat{\boldsymbol{k}}\, Y^*_{\ell m}(\hat{\boldsymbol{k}})\, \delta(\boldsymbol{k})\,, \end{aligned} \tag{4}$$

where the orthogonality relations Eqs. (A6) and (A7) were used. Eq. (4) shows that SFB is a spherical harmonic transform of Cartesian Fourier modes with an additional phase factor i^ℓ. And

$$\delta(\boldsymbol{k}) = \frac{(2\pi)^{\frac{3}{2}}}{k} \sum_{\ell m} i^{-\ell}\, Y_{\ell m}(\hat{\boldsymbol{k}})\, \delta_{\ell m}(k) \tag{5}$$

is the inverse of Eq. (4).

A. The Homogeneous and Isotropic Universe

In a homogeneous and isotropic universe in real-space (with no line-of-sight effects), we have

$$\left\langle \delta(\boldsymbol{k})\, \delta^*(\boldsymbol{k}') \right\rangle = (2\pi)^3 \delta^D(\boldsymbol{k} - \boldsymbol{k}')\, P(k)\,. \tag{6}$$

Therefore, applying Eq. (4) gives the SFB power spectrum as

$$\left\langle \delta_{\ell m}(k)\, \delta^*_{\ell' m'}(k') \right\rangle = \delta^D(k - k')\, \delta^K_{\ell\ell'}\, \delta^K_{mm'}\, P(k)\,, \tag{7}$$

where we used Eq. (A2) for the three-dimensional Dirac-delta function in spherical coordinates. That is, in a homogeneous and isotropic universe with no observational effects the SFB power spectrum equals the 3D power spectrum $P(k)$.

B. The Linear Universe

We now generalize to include line-of-sight effects, a linearly evolving power spectrum, and a radial window function. The galaxy density contrast we consider is

$$\begin{aligned}\delta_g^{\mathrm{obs}}(\boldsymbol{r}) &= W(\boldsymbol{r})\, D(r) \int \frac{\mathrm{d}^3 q}{(2\pi)^3}\, e^{i\boldsymbol{q}\cdot\boldsymbol{r}}\, \widetilde{A}_{\mathrm{RSD}}(\mu, q\mu, r) \\ &\quad \times b(r, q)\, \delta(\boldsymbol{q})\,, \end{aligned} \tag{8}$$

where $\delta(\boldsymbol{q})$ is the matter density contrast in Fourier space, $W(\boldsymbol{r})$ is the survey window function, $D(r)$ is the linear growth factor, $b(r, q)$ is the possibly scale-dependent linear galaxy bias, $\mu = \hat{\boldsymbol{q}} \cdot \hat{\boldsymbol{r}}$, and the redshift-space distortions are encoded in

$$\widetilde{A}_{\mathrm{RSD}}(\mu, q\mu, r) = \left(1 + \beta\mu^2\right) \widetilde{A}_{\mathrm{FoG}}(q\mu)\,, \tag{9}$$

with $\beta = f/b$, where $f = \mathrm{d}\ln D/\mathrm{d}\ln a$ is the linear growth rate, and we assume a Gaussian fingers-of-God term

$$\widetilde{A}_{\mathrm{FoG}}(q\mu) = e^{-\frac{1}{2}\sigma_u^2 q^2 \mu^2}\,, \tag{10}$$

with $\sigma_u = \sigma_v/aH$ the pair-wise velocity dispersion in units of length. The tilde on A_{RSD} signifies that it is a Fourier-space function.

The RSD term $\widetilde{A}_{\mathrm{RSD}}$ in Eq. (8) can be expressed as a function of derivatives on the complex exponential. That is, by performing a Taylor series expansion we can replace $\mu \to -i\partial_{qr}$, or

$$\begin{aligned}\widetilde{A}_{\mathrm{RSD}}(\mu, q\mu, r)\, e^{i\boldsymbol{q}\cdot\boldsymbol{r}} &= \sum_n \frac{a_n(q, r)}{n!}\, \mu^n\, e^{iqr\mu} \\ &= \sum_n \frac{a_n(q, r)}{n!} \left(-i\, \frac{\partial}{\partial(qr)}\right)^n e^{iqr\mu} \\ &= \widetilde{A}_{\mathrm{RSD}}(-i\partial_{qr}, -iq\partial_{qr}, r)\, e^{i\boldsymbol{q}\cdot\boldsymbol{r}}\,. \end{aligned} \tag{11}$$

Furthermore, the complex exponential is expanded using Rayleigh's formula Eq. (A10) so that the derivatives in $\widetilde{A}_{\mathrm{RSD}}$ only act on the spherical Bessel function from Rayleigh's formula. Further expressing the Fourier-space density contrast in terms of its SFB modes Eq. (5), the observed density contrast Eq. (8) now becomes

$$\begin{aligned}\delta_g^{\mathrm{obs}}(\boldsymbol{r}) &= W(\boldsymbol{r})\, D(r) \int \frac{\mathrm{d}^3 q}{(2\pi)^3}\, b(r, q) \left[\widetilde{A}_{\mathrm{RSD}}(-i\partial_{qr}, -iq\partial_{qr}, r)\, 4\pi \sum_{L_1 M_1} i^{L_1} j_{L_1}(qr)\, Y^*_{L_1 M_1}(\hat{\boldsymbol{q}})\, Y_{L_1 M_1}(\hat{\boldsymbol{r}})\right] \\ &\quad \times \frac{(2\pi)^{\frac{3}{2}}}{q} \sum_{LM} i^{-L}\, Y_{LM}(\hat{\boldsymbol{q}})\, \delta_{LM}(q) \end{aligned} \tag{12}$$

$$= W(\boldsymbol{r})\, D(r) \sqrt{\frac{2}{\pi}} \int \mathrm{d}q\, q^2\, b(r, q) \left[\widetilde{A}_{\mathrm{RSD}}(-i\partial_{qr}, -iq\partial_{qr}, r) \sum_{LM} j_L(qr)\, Y_{LM}(\hat{\boldsymbol{r}})\right] \frac{1}{q}\, \delta_{LM}(q)\,. \tag{13}$$

Using Eq. (2) to transform into SFB space,

$$\delta^{g,\rm obs}_{\ell m}(k) = \int {\rm d}q \sum_{LM} \mathcal{W}^{LM}_{\ell m}(k,q)\, \delta_{LM}(q)\,, \tag{14}$$

where

$$\mathcal{W}^{LM}_{\ell m}(k,q) = \int {\rm d}^2\hat{\boldsymbol{r}}\, Y_{LM}(\hat{\boldsymbol{r}})\, Y^*_{\ell m}(\hat{\boldsymbol{r}})\, \mathcal{W}^{L}_{\ell}(k,q,\hat{\boldsymbol{r}})\,, \tag{15}$$

and

$$\begin{aligned}\mathcal{W}^{L}_{\ell}(k,q,\hat{\boldsymbol{r}}) = \frac{2qk}{\pi} \int {\rm d}r\, r^2\, W(\boldsymbol{r})\, D(r)\, b(r,q)\, j_\ell(kr) \\ \times\, \widetilde{A}_{\rm RSD}(-i\partial_{qr}, -iq\partial_{qr}, r) j_L(qr)\,.\end{aligned} \tag{16}$$

The SFB correlation function is, therefore,

$$\begin{aligned}&\left\langle \delta^{g,\rm obs}_{\ell m}(k)\, \delta^{g,\rm obs,*}_{\ell' m'}(k') \right\rangle \\ &= \int {\rm d}q \sum_{LM} \mathcal{W}^{LM}_{\ell m}(k,q)\, \mathcal{W}^{LM,*}_{\ell' m'}(k',q)\, P(q)\,,\end{aligned} \tag{17}$$

where we used Eqs. (7) and (14).

Here we will only consider a radial selection function, as the angular mask will be handled in the estimator. Then,

$$W(\boldsymbol{r}) = \phi(r)\,, \tag{18}$$

and we define the simplification of Eq. (16)

$$\mathcal{W}_\ell(k,q) = \mathcal{W}^{\ell}_{\ell}(k,q,\hat{\boldsymbol{r}})\,, \tag{19}$$

which is then independent of the direction $\hat{\boldsymbol{r}}$. Eq. (15) and Eq. (17) then simplify to

$$\left\langle \delta^{g,\rm obs}_{\ell m}(k)\, \delta^{g,\rm obs,*}_{\ell' m'}(k') \right\rangle = \delta^K_{\ell\ell'} \delta^K_{mm'}\, C_\ell(k,k')\,, \tag{20}$$

with the SFB power spectrum defined as

$$C_\ell(k,k') = \int {\rm d}q\, \mathcal{W}_\ell(k,q)\, \mathcal{W}^*_\ell(k',q)\, P(q)\,. \tag{21}$$

Eqs. (16), (19) and (21) show that RSD and linear growth can be taken into account by a change in the radial window function.

Note that for a homogeneous and isotropic universe without selection function, $W(\boldsymbol{r}) = D(r) = \widetilde{A}_{\rm RSD} = 1$ and $b(r,q) = $ const, the window becomes $\mathcal{W}_\ell(k,q) = \delta^D(k-q)$, and Eq. (7) is reproduced. Also, note that $\mathcal{W}_\ell(k,q)$ is real, because the imaginary parts only appear with even powers in $\widetilde{A}_{\rm RSD}$.

C. Limber's Approximation

In this section we aim to gain intuition for the SFB power spectrum in Eq. (21) by applying Limber's approximation. To do so, we will also approximate the effect of the FoG. We write Eqs. (9) and (10) acting on a spherical Bessel function as

$$\begin{aligned}&\widetilde{A}_{\rm RSD}(-iq\partial_{qr}, -i\partial_{qr}, r)\, j_\ell(qr) \\ &= e^{\frac{1}{2}\sigma_u^2 q^2 \partial^2_{qr}} \left(1 - \beta\partial^2_{qr}\right) j_\ell(qr)\,.\end{aligned} \tag{22}$$

The second derivative is obtained exactly via a recursion relation for the derivative of Spherical Bessel function,

$$\begin{aligned}\left(1-\beta\partial^2_{qr}\right) j_\ell(qr) &= \left(1-\beta f^\ell_0\right) j_\ell(qr) - \beta f^\ell_{-2}\, j_{\ell-2}(qr) \\ &\quad - \beta f^\ell_2\, j_{\ell+2}(qr) \qquad (23)\\ &= \sum_{\Delta\ell} \left(\delta^K_{\Delta\ell,0} - \beta f^\ell_{\Delta\ell}\right) j_{\ell+\Delta\ell}(qr)\,, \qquad (24)\end{aligned}$$

where the only non-zero $f^\ell_{\Delta\ell}$ are

$$f^\ell_{-2} = \frac{\ell(\ell-1)}{(2\ell-1)(2\ell+1)}\,, \tag{25}$$

$$f^\ell_0 = -\frac{2\ell^2+2\ell-1}{(2\ell-1)(2\ell+3)}\,, \tag{26}$$

$$f^\ell_2 = \frac{(\ell+1)(\ell+2)}{(2\ell+1)(2\ell+3)}\,. \tag{27}$$

The FoG term acting on the spherical Bessel function is a convolution

$$\begin{aligned}\widetilde{A}_{\rm FoG}(-iq\partial_{qr})\, j_\ell(qr) &= \int \frac{{\rm d}k}{2\pi}\, e^{ikqr}\, \widetilde{A}_{\rm FoG}(qk)\, \widetilde{j}_\ell(k) \\ &= \int {\rm d}y\, A_{\rm FoG}(r-y)\, j_\ell(qy) \qquad (28)\\ &= \int {\rm d}y\, \frac{1}{\sqrt{2\pi}\,\sigma_u}\, e^{-\frac{(r-y)^2}{2\sigma_u^2}}\, j_\ell(qy)\,, \qquad (29)\end{aligned}$$

where the tilde signify Fourier transforms, and we took the inverse transform of Eq. (10) (see e.g. Grasshorn Gebhardt and Jeong 2020). As a first approximation, if the frequency q is low, then the convolution will have little effect. If the frequency is high, the convolution will erase the oscillations to vanish. That is, we approximate

$$\widetilde{A}_{\rm FoG}(-iq\partial_{qr})\, j_\ell(qr) \approx e^{-\frac{1}{2}\sigma_u^2 q^2}\, j_\ell(qr)\,. \tag{30}$$

We are now in a position to apply Limber's approximation (LoVerde and Afshordi 2008)

$$j_\ell(kr) \to \sqrt{\frac{\pi}{2kr}}\, \delta^D\left(kr - \ell - \frac{1}{2}\right)\,. \tag{31}$$

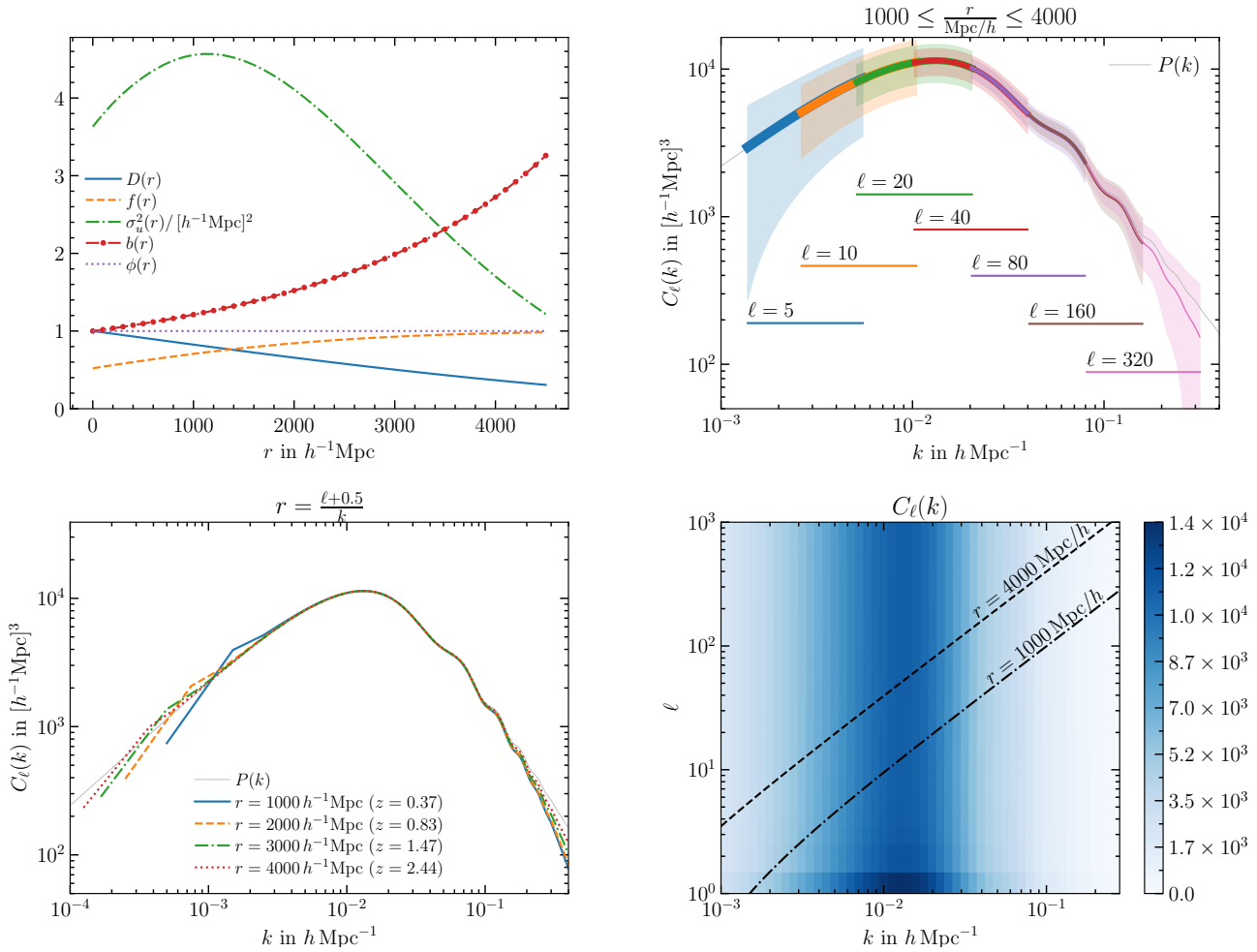

FIG. 1. Top left: Linear growth factor $D(r)$, linear growth rate $f(r)$, velocity dispersion $\sigma_u^2 = \sigma_v^2/(aH)^2$, galaxy bias $b(r) = b_0/D(r)$ where $b_0 = 1$, and selection function $\phi(r)$ defined in Eq. (18). Top right: The SFB power spectrum in the Limber approximation closely traces the 3D power spectrum. However, for a given perpendicular mode ℓ and redshift range, only a part of the power spectrum is measured. The horizontal lines show the range of k modes that a given ℓ mode is able to measure for a survey within $1000 \leqslant \frac{r}{h^{-1}\mathrm{Mpc}} \leqslant 4000$, and the shaded bands show an estimate for the 1σ measurement uncertainty for that particular ℓ-mode. Bottom left: Here, each line fixes the redshift, and all ℓ modes are used. The Kaiser effect is not visible due to the Limber approximation becoming invalid on large scales. Bottom right: Here we show the SFB power spectrum on a grid of ℓ-k modes. The SFB power spectrum can be measured within a band such that $r \simeq \left(\ell + \frac{1}{2}\right)/k$ is within the survey.

Then, Eqs. (16) and (19) become

$$\begin{aligned}\mathcal{W}_\ell(k,q) &= \frac{2qk}{\pi}\int \mathrm{d}r\, r^2\, \phi(r)\, D(r)\, b(r,q)\, j_\ell(kr) \\ &\quad\times\, e^{-\frac{1}{2}\sigma_u^2 q^2} \sum_{\Delta\ell} \left(\delta^K_{\Delta\ell,0} - \beta f^\ell_{\Delta\ell}\right) j_{\ell+\Delta\ell}(qr) \quad (32)\\ &= \sqrt{\frac{q}{k}}\,\phi\left(\frac{\ell+\frac{1}{2}}{k}\right) D\left(\frac{\ell+\frac{1}{2}}{k}\right) b\left(\frac{\ell+\frac{1}{2}}{k}, q\right) \\ &\quad\times\, e^{-\frac{1}{2}\sigma_u^2 q^2} \sum_{\Delta\ell} \left(\delta^K_{\Delta\ell,0} - \beta f^\ell_{\Delta\ell}\right) \\ &\quad\times\, \delta^D\left(q - \frac{\ell+\Delta\ell+\frac{1}{2}}{\ell+\frac{1}{2}}\,k\right). \quad (33)\end{aligned}$$

Since the Limber approximation is only applicable for large ℓ, we further assume $\Delta\ell \ll \ell$. Then,

$$\begin{aligned}\mathcal{W}_\ell(k,q) &= \delta^D(q-k)\,\phi\left(\frac{\ell+\frac{1}{2}}{k}\right) D\left(\frac{\ell+\frac{1}{2}}{k}\right) b\left(\frac{\ell+\frac{1}{2}}{k}, k\right) \\ &\quad\times\, e^{-\frac{1}{2}\sigma_u^2 k^2} \sum_{\Delta\ell} \left(\delta^K_{\Delta\ell,0} - \beta f^\ell_{\Delta\ell}\right). \quad (34)\end{aligned}$$

Therefore, the SFB power spectrum Eq. (21) in the Lim-

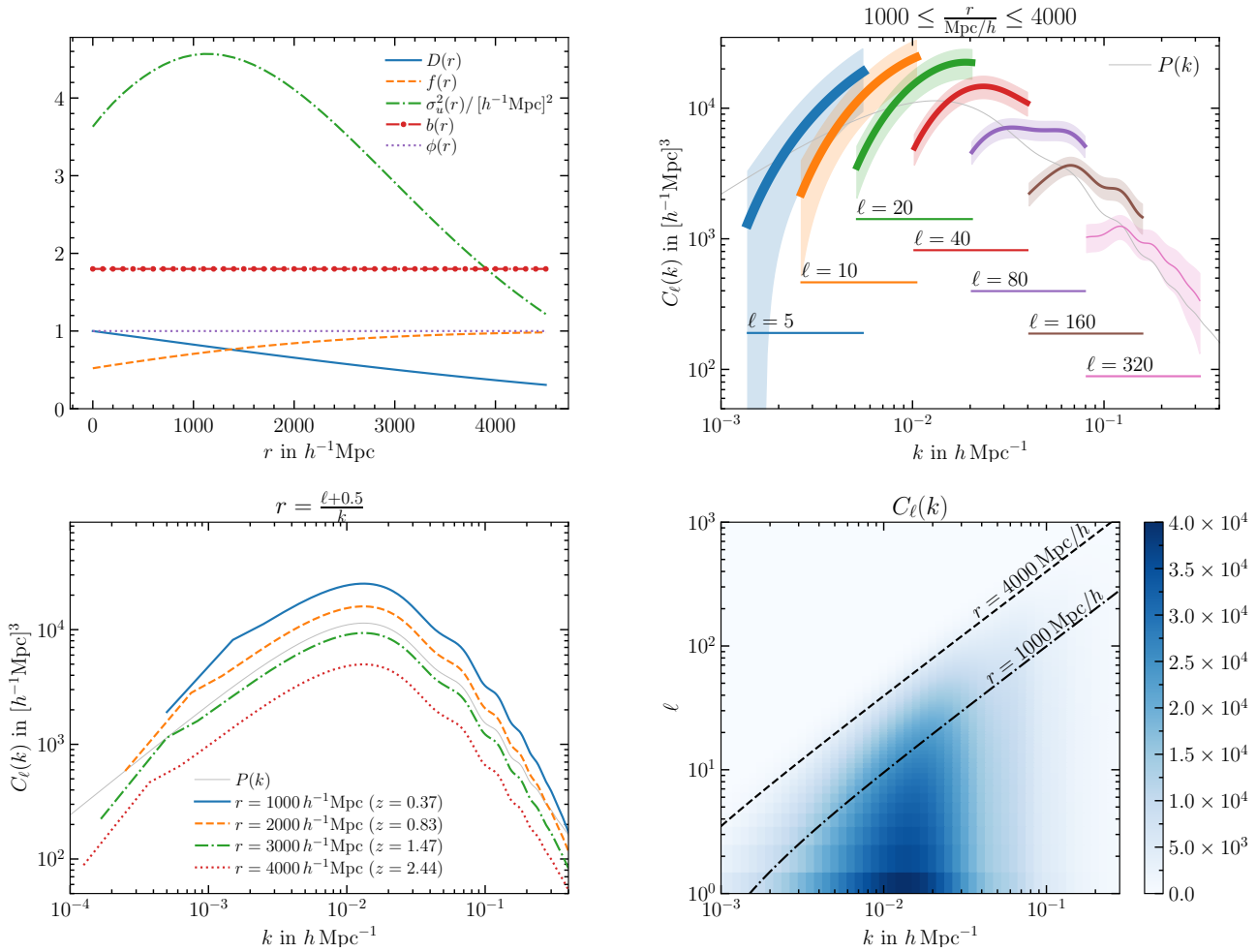

FIG. 2. Same as Fig. 1, except that the linear galaxy bias is now constant $b(r) = 1.8$. As a result, the redshift evolution of the linear growth factor $D(r)$ is no longer cancelled by the bias. Top right: At a fixed ℓ, larger-scale modes are probed at higher redshift where the growth factor is smaller. Thus, compared to Fig. 1, each ℓ-segment appears tilted. Bottom left: The redshift evolution of the linear growth factor $D(r)$ causes a shift in the power spectrum amplitude with the Limber ratio $r = (\ell + \frac{1}{2})/k$. Bottom right: High-$\ell$ modes are suppressed because they primarily probe the high redshifts.

ber approximation is

$$C_\ell(k,k') = P(k)\, e^{-\sigma_u^2 k^2}\, \delta^D(k-k') \times \phi^2\left(\frac{\ell+\frac{1}{2}}{k}\right) D^2\left(\frac{\ell+\frac{1}{2}}{k}\right) b^2\left(\frac{\ell+\frac{1}{2}}{k}, k\right) \times \left[1 - \beta\left(f^\ell_{-2} + f^\ell_0 + f^\ell_2\right)\right]^2 . \quad (35)$$

The exponential is the suppression due to the FoG. The Dirac-delta function shows that even with redshift-evolution most of the power is on the diagonal $k = k'$, as for a non-evolving universe. Redshift evolution manifests itself mainly through the interplay between ℓ and k such that in the Limber approximation the ratio

$$r = \frac{\ell+\frac{1}{2}}{k} \quad (36)$$

is the comoving angular diameter distance. For example, if the scale k is fixed, then changing the angular scale ℓ corresponds to changing the redshift. We note that primordial non-Gaussianity will lead to a scale-dependent bias that will be absorbed directly in the bias term on the second line. Finally, the last line in Eq. (35) accounts for the linear Kaiser effect.

In Fig. 1 we show the SFB power spectrum in the Limber approximation. We define $C_\ell(k,k) = \delta^D(k-k')\, C_\ell(k)$. For the galaxy bias we choose $b(r,k) = b_0/D(r)$ with $b_0 = 1$ so that the bias and linear growth factor cancel, and our selection function is a constant $\phi(r) = 1$ for illustration. The top left panel shows the inputs to our calculation.

The top right panel of Fig. 1 shows the SFB power spectrum for several fixed ℓ modes. The shaded areas correspond to the 1σ measurement uncertainty estimated

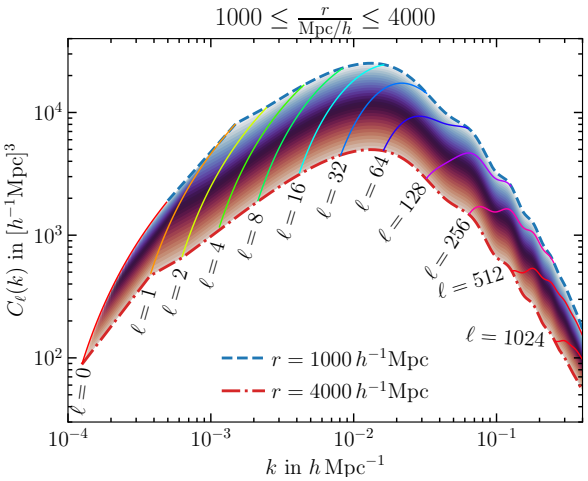

FIG. 3. Here we combine the top right and bottom left plots in Fig. 2 to show the region that the SFB power spectrum probes in the Limber approximation for a given redshift range and linear power spectrum evolution.

via

$$\Delta C_\ell(k) = \sqrt{\frac{2}{2\ell+1}}\left(C_\ell(k) + \frac{1}{\bar{n}}\right), \tag{37}$$

(Pratten and Munshi 2013). Since ℓ corresponds to perpendicular wave modes, at small r the corresponding k modes are large, and at large r the corresponding k modes are small. Therefore, at a constant ℓ, the SFB power spectrum as a function of k sweeps through both redshift and k modes, measuring a redshift corresponding to $r \simeq 4000\,h^{-1}$ Mpc at lower k, and a redshift corresponding to $r \simeq 1000\,h^{-1}$ Mpc at higher k.

Consequently, in the ℓ-k plane, only a band of modes can be measured, as illustrated in the bottom right plot of Fig. 1. Fixing the redshift, which is possible in the Limber approximation, results in a bona-fide power spectrum measurement, as illustrated in the bottom left panel.

In the Limber approximation, the SFB power spectrum does not exhibit a strong Kaiser effect on large scales. We attribute this to the fact that Limber's approximation is valid only in the small-scale limit where the Kaiser effect is negligible.

Because Eq. (36) relates the ℓ and k modes to a definite redshift, we can only measure a band of modes. We illustrate this in the bottom right panel of Fig. 1.

The choice $b(r,q) \propto D^{-1}(r)$ results in linear bias and linear growth cancelling each other. In general, this may not be the case, and we illustrate redshift evolution by setting the bias constant, $b(r,q) = 1.8$, in Fig. 2. Because for fixed ℓ larger-scale modes k correspond to higher redshift, the linear growth evolution tilts each ℓ-segment of the power spectrum in the top right panel. The bottom left panel shows the power spectrum at fixed redshift according to the Limber ratio Eq. (36), sweeping through ℓ.

Each segment in the top right panel of Fig. 2 crosses the lines in the bottom left panel. We illustrate this further in Fig. 3.

III. SFB DECOMPOSITION

This section describes our SFB decomposition for a galaxy survey with mask and selection function. We largely follow Samushia (2019) for the radial basis functions and Leistedt *et al.* (2012) for the angular/radial split in the estimator.

We start by giving a review of the basis functions, then we add window and selection functions, we model the discrete galaxy distribution, and estimate the covariance matrix.

A. Spherical Fourier-Bessel basis with potential boundary conditions

As noted in the introduction, we choose the eigenbasis of the Laplacian because that makes scalar modes independent to first order in cosmological perturbation theory (Bernardeau *et al.* 2002). Here, we lay out the boundary conditions we consider similar to Samushia (2019). However, as observers fixed in one location, using light that travels at a finite speed, it is more natural to use spherical polar coordinates that separate the radial and angular observations. Then, the Laplacian on a scalar function f becomes

$$\nabla^2 f = \frac{1}{r^2}\frac{\partial}{\partial r}\left(r^2\frac{\partial f}{\partial r}\right) + \frac{1}{r^2\sin\theta}\frac{\partial}{\partial\theta}\left(\sin\theta\frac{\partial f}{\partial\theta}\right) + \frac{1}{r^2\sin^2\theta}\frac{\partial^2 f}{\partial\phi^2}, \tag{38}$$

where r, θ, and ϕ are the comoving angular diameter distance, zenith angle, and azimuthal angle, respectively (see Appendix B for a derivation). The eigenbasis to Eq. (38) that satisfies

$$\nabla^2 f = -k^2 f \tag{39}$$

for some mode k is of the form (see e.g. Samushia 2019)

$$\begin{aligned} f_{\ell\mu}(k;r,\theta,\phi) = &\left[c_j\, j_\ell(kr) + c_y\, y_\ell(kr)\right] \\ &\times \left[c_p\, P_\ell^\mu(\cos\theta) + c_q\, Q_\ell^\mu(\cos\theta)\right] \\ &\times \left[c_+\, e^{i\mu\phi} + c_-\, e^{-i\mu\phi}\right], \end{aligned} \tag{40}$$

where the c_i are constants, and j_ℓ and y_ℓ are spherical Bessel functions of the first and second kind, and P_ℓ^μ and Q_ℓ^μ are Legendre functions of the first and second kind.

The constants c_i are set by boundary conditions. First, the spherical Bessel of the second kind, y_ℓ diverges with vanishing argument; hence, typically $c_y = 0$. Typically, the functions also need to be periodic about the azimuthal angle ϕ; therefore, $\mu = 0, 1, 2, \ldots$ is an integer.

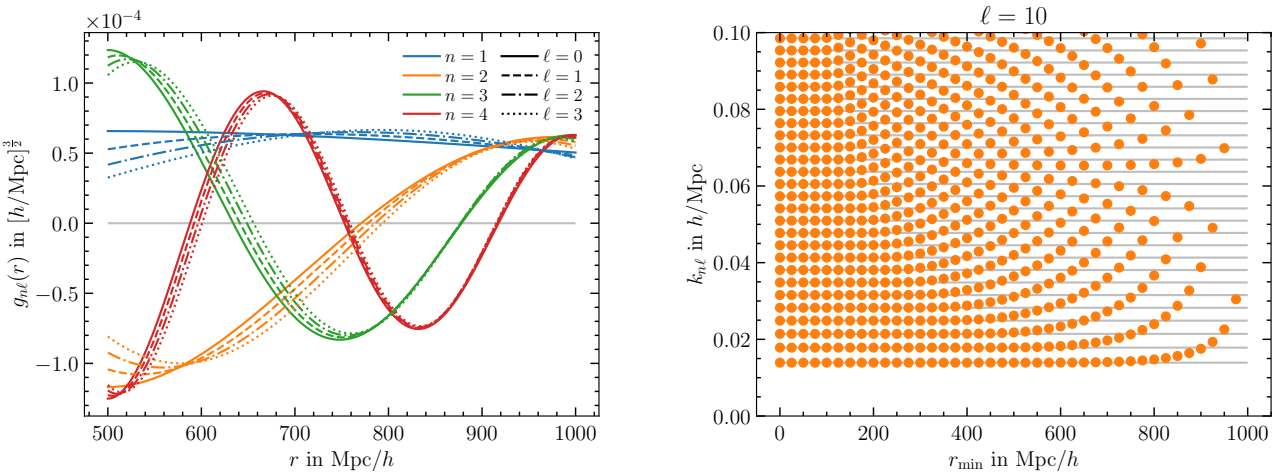

FIG. 4. Left: The radial basis functions for potential boundary conditions as a function of r. Color indicates the modes n, line style indicates ℓ as shown in the legend. Here, $r_{\rm min} = 500\,h^{-1}\,$Mpc and $r_{\rm max} = 1000\,h^{-1}\,$Mpc. Right: $k_{n\ell}$ for potential boundary conditions as a function of $r_{\rm min}$ when $\ell = 10$. The grey lines are for $r_{\rm min} = 0$, and we fix $r_{\rm max} = 1000\,h^{-1}\,$Mpc.

Then, the functions also need to be finite for $\cos\theta = \pm 1$, typically; therefore, $c_q = 0$, and $\ell = 0, 1, 2, \ldots$ is an integer, and $-\ell \leqslant \mu \leqslant \ell$.

Effectively, the preceding paragraph imposed boundary conditions at $r_{\rm min} = 0$ and assumed coverage of the whole sky. Typically (e.g., Heavens and Taylor 1995, Tadros *et al.* 1999, Percival *et al.* 2004, Fisher *et al.* 1995), one would then go ahead and also impose boundary conditions at some $r_{\rm max}$ such that the survey volume is contained within a sphere of radius $r_{\rm max}$. This restricts the SFB volume, i.e., the volume on which the SFB transform is performed, as the region from $0 \leqslant r \leqslant r_{\rm max}$. Demanding the basis functions to be orthogonal then leads to a discrete spectrum of modes $k = k_{n\ell}$.

Realistic galaxy surveys do not occupy the entire SFB volume, but are restricted in both redshift and angular area, and, therefore, they leave large fractions of the SFB volume unobserved. This leads to the deconvolution of the window function to be numerically unstable. It also results in wasted computational resources if the survey covers only a (potentially thick) shell at high redshift. The analogous picture for a standard Fourier transform would be to have a transform box that is much larger than the survey volume. Therefore, the selection function will vanish for part of the SFB volume, and, because in that case some modes are not well constrained, the inversion of the window function becomes numerically unstable.

In this paper, we employ two strategies to deal with this problem. First, we follow Hivon *et al.* (2002), Alonso *et al.* (2019) and bin the pseudo SFB power spectrum into bandpowers. This combines several poorly-constrained modes into one well-constrained mode. We rely on this strategy especially for the angular mask so that we can leverage the full-sky spherical harmonic algorithms from the `HealPy` software (Górski *et al.* 2005, Zonca *et al.* 2019).

For the second strategy, we follow Samushia (2019) and move the boundary at the origin to some $r_{\rm min}$ so that the SFB volume extends from $r_{\rm min} \leqslant r \leqslant r_{\rm max}$. For galaxy surveys that start at some minimum redshift this eliminates from the SFB tranform volume a hole around the origin. As a result, the inversion of the window function is numerically well behaved even without resorting to bandpower binning. Furthermore, the number of SFB modes is reduced not just by the boundary condition at $r_{\rm max}$, but the boundary condition at $r_{\rm min}$ also reduces the number of modes further by the fraction $r_{\rm min}^3/r_{\rm max}^3$. In all cases considered in this paper, this eliminates the need for bandpower binning in the radial direction.

We differ from Samushia (2019) in that we use potential boundary conditions (Fisher *et al.* 1995) that ensure the field represented by the SFB decomposition is continuous and smooth at the boundary. These boundary conditions lead to a spectrum of modes $k_{n\ell}$, as shown in Appendix C. In the appendix we also derive that the radial basis functions with such boundary conditions become a linear combination of spherical Bessels of the first and second kind,

$$g_{n\ell}(r) = c_{n\ell}\, j_\ell(k_{n\ell}\, r) + d_{n\ell}\, y_\ell(k_{n\ell}\, r)\,, \tag{41}$$

which satisfy an orthonormality relation

$$\int_{r_{\rm min}}^{r_{\rm max}} {\rm d}r\, r^2\, g_{n\ell}(r)\, g_{n'\ell}(r) = \delta^K_{nn'}\,, \tag{42}$$

where $\delta^K_{nn'}$ is a Kronecker delta, and the coefficients $c_{n\ell}$ and $d_{n\ell}$ are derived in Appendix C. With Eq. (42), the Fourier pair Eqs. (1) and (2) remains a Fourier pair with

the discrete $k_{n\ell}$-spectrum, and the pair becomes

$$\delta(\boldsymbol{r}) = \sum_{n\ell m} \Big[g_{n\ell}(r)\, Y_{\ell m}(\hat{\boldsymbol{r}}) \Big] \delta_{n\ell m}\,, \tag{43}$$

$$\delta_{n\ell m} = \int \mathrm{d}^3\boldsymbol{r} \Big[g_{n\ell}(r)\, Y^*_{\ell m}(\hat{\boldsymbol{r}}) \Big] \delta(\boldsymbol{r})\,, \tag{44}$$

where $\delta_{n\ell m} = \delta_{\ell m}(k_{n\ell})$. Note that our choice to normalize $g_{n\ell}(r)$ as in Eq. (42) changes the units of $\delta_{n\ell m}$ compared to Eqs. (1) and (2). In effect, this choice of units takes into account the survey volume at this stage rather than at the stage of forming the correlation function.

Examples of the resulting basis functions and modes $k_{n\ell}$ are show in Fig. 4. We point out that the $\ell = 0$ modes are closely related to taking the average of the transformed field $\delta(\boldsymbol{r})$. Also, a larger $r_{\rm min}$ results in a smaller volume, and, therefore, fewer modes that can be constrained.

B. Window and selection function

The observed number density $n(\boldsymbol{r})$ of galaxies is subject to the window and selection function $W(\boldsymbol{r})$ of the survey, which we define as the fraction of galaxies observed at position $\boldsymbol{r}$. For a random catalogue subject to the same window function, with density $n_r(\boldsymbol{r})$, and with $1/\alpha$ as many galaxies as the survey, we then have

$$\alpha \langle n_r(\boldsymbol{r}) \rangle = W(\boldsymbol{r})\, \bar{n}\,, \tag{45}$$

where $\langle n_r(\boldsymbol{r}) \rangle = \alpha^{-1} \bar{n}(\boldsymbol{r})$ is the average number density of the ensemble of random catalogs, and $\bar{n}$ is the average number density in the survey. Note that Eq. (45) can equivalently be expressed in terms of the limit $\lim_{\alpha\to 0} \alpha\, n_r(\boldsymbol{r}) = \bar{n}(\boldsymbol{r}) = W(\boldsymbol{r})\, \bar{n}$. With this definition of the window function, we define the effective volume as

$$V_{\rm eff} = \int \mathrm{d}^3\boldsymbol{r}\, W(\boldsymbol{r})\,, \tag{46}$$

so that the average number density $\bar{n}$ becomes

$$\bar{n} = \frac{N^{\rm obs}_{\rm gal}}{V_{\rm eff}}\,, \tag{47}$$

and $N^{\rm obs}_{\rm gal}$ is the observed number of galaxies in the survey. Any variation across the survey in the actual average number density, e.g., due to an evolving luminosity function, is absorbed into $W(\boldsymbol{r})$. Our treatment is in line with Taruya *et al.* (2021), and our $W(\boldsymbol{r})$ takes the role of the function $G(\boldsymbol{r})$ in Feldman *et al.* (1994), except that we do not at present include a weighting scheme.

In a sense, there are two window functions here: first, the one defined by the SFB procedure and limited by $r_{\rm min} \leqslant r \leqslant r_{\rm max}$, and second, $W(\boldsymbol{r})$, which defines the geometry and selection of the survey. However, the first one should be irrelevant as long as the survey volume is entirely inside $r_{\rm min} \leqslant r \leqslant r_{\rm max}$ and as along as sufficient number of modes are included in the SFB analysis.

The observed density fluctuation field is, then,

$$\delta^{\rm obs}(\boldsymbol{r}) = \frac{n(\boldsymbol{r}) - \alpha\, n_r(\boldsymbol{r})}{\bar{n}} = \frac{n(\boldsymbol{r})}{\bar{n}} - W(\boldsymbol{r})\,, \tag{48}$$

where Eq. (45) was used in the limit that the random catalogue has an infinite number of galaxies, or $\alpha \to 0$. Because the observed density $n(\boldsymbol{r})$ is also subject to the window function $W(\boldsymbol{r})$, the observed and true density contrasts are related by

$$\delta^{\rm obs}(\boldsymbol{r}) = W(\boldsymbol{r})\, \delta^A(\boldsymbol{r})\,, \tag{49}$$

where we attach the superscript 'A' to refer to the local average effect (see Section III H below). Transforming to SFB-space and expressing $\delta^A(\boldsymbol{r})$ in terms of its SFB decomposition Eqs. (43) and (44), we get

$$\delta^{\rm obs}_{n\ell m} = \sum_{n'\ell'm'} W^{n'\ell'm'}_{n\ell m}\, \delta^A_{n'\ell'm'}\,, \tag{50}$$

where

$$W^{n'\ell'm'}_{n\ell m} = \int \mathrm{d}r\, r^2\, g_{n\ell}(r)\, g_{n'\ell'}(r) \times \int \mathrm{d}^2\hat{\boldsymbol{r}}\, Y^*_{\ell m}(\hat{\boldsymbol{r}})\, Y_{\ell' m'}(\hat{\boldsymbol{r}})\, W(r, \hat{\boldsymbol{r}})\,. \tag{51}$$

1. *Properties and implementation*

From Eq. (51) follows the symmetry

$$W^{n',\ell',-m'}_{n,\ell,m} = (-1)^{m+m'} W^{n',\ell',m',*}_{n,\ell,-m}\,, \tag{52}$$

and the Hermitian property

$$W^{n'\ell'm'}_{n\ell m} = W^{n\ell m,*}_{n'\ell'm'}\,. \tag{53}$$

In the special case that $W(\boldsymbol{r}) = 1$ everywhere,

$$W^{n'\ell'm'}_{n\ell m} = \delta^K_{nn'} \delta^K_{\ell\ell'} \delta^K_{mm'}\,, \tag{54}$$

which follows from Eq. (42) and Eq. (A7).

In all generality, Eq. (51) can be simplified for computational convenience by expressing the window function in terms of an angular transform. That is, introduce

$$W_{LM}(r) = \int \mathrm{d}^2\hat{\boldsymbol{r}}\, Y^*_{LM}(\hat{\boldsymbol{r}})\, W(r, \hat{\boldsymbol{r}})\,. \tag{55}$$

Then,

$$W^{n'\ell'm'}_{n\ell m} = (-1)^m \sum_L \mathcal{G}^{\ell\ell' L}_{-m,m',m-m'} \times \int \mathrm{d}r\, r^2\, g_{n\ell}(r)\, g_{n'\ell'}(r)\, W_{L,m-m'}(r)\,, \tag{56}$$

where we used Eq. (A12) and introduced the Gaunt factor Eq. (A14). In writing Eq. (56) we performed the angular transform of the window function only as that leads to a computationally suitable form. Had we performed a full SFB transform, we would have been left with an infinite sum over n that converges slowly, in addition to the need of computing integrals over three spherical Bessel functions.

C. Discrete points

Now we specialize the SFB decomposition to the case that we have galaxies represented by discrete points. That is, we assume the number density is given by

$$n(\boldsymbol{r}) = \sum_p \delta^D(\boldsymbol{r} - \boldsymbol{r}_p)\,, \tag{57}$$

where the sum is over all points (galaxies) in the survey.

In the 3DEX approach (Leistedt *et al.* 2012), which we adopt here, Eq. (44) is decomposed into its radial and angular integrals, and the radial integration is performed first. That is,

$$\delta^{\rm obs}_{n\ell m} = \int \mathrm{d}^2\Omega_{\hat{\boldsymbol{r}}}\, Y^*_{\ell m}(\hat{\boldsymbol{r}})\, \delta^{\rm obs}_{n\ell}(\hat{\boldsymbol{r}})\,, \tag{58}$$

where

$$\delta^{\rm obs}_{n\ell}(\hat{\boldsymbol{r}}) = \int_{r_{\rm min}}^{r_{\rm max}} \mathrm{d}r\, r^2\, g_{n\ell}(r)\, \delta^{\rm obs}(r, \hat{\boldsymbol{r}}) \tag{59}$$

represents an angular field for each n and ℓ, and $g_{n\ell}$ is defined in Eq. (41). For the density contrast Eq. (48) with number density Eq. (57),

$$\delta^{\rm obs}_{n\ell}(\hat{\boldsymbol{r}}) = \frac{1}{\bar{n}} \sum_p \delta^D(\hat{\boldsymbol{r}} - \hat{\boldsymbol{r}}_p)\, g_{n\ell}(r_p) - W_{n\ell}(\hat{\boldsymbol{r}})\,, \tag{60}$$

where

$$W_{n\ell}(\hat{\boldsymbol{r}}) = \int_{r_{\rm min}}^{r_{\rm max}} \mathrm{d}r\, r^2\, g_{n\ell}(r)\, W(\boldsymbol{r})\,. \tag{61}$$

Eq. (60) is an exact expression for the observed density contrast $\delta^{\rm obs}_{n\ell}(\hat{\boldsymbol{r}})$. However, for the angular transform we wish to make use of the fast HEALPix scheme[1,2], and we need the density contrast in pixel i averaged over the pixel area $\Delta\Omega_i$,

$$\bar{\delta}^{\rm obs}_{n\ell}(\hat{\boldsymbol{r}}_i) = \frac{1}{\Delta\Omega_i} \int_{\Delta\Omega_i} \mathrm{d}\Omega_{\hat{\boldsymbol{r}}}\, \delta^{\rm obs}_{n\ell}(\hat{\boldsymbol{r}}) \tag{62}$$

$$= \frac{1}{\bar{n}\Delta\Omega_i} \sum_{p\in\Delta\Omega_i} g_{n\ell}(r_p) - W_{n\ell}(\hat{\boldsymbol{r}}_i)\,, \tag{63}$$

where we assumed that $W_{n\ell}(\hat{\boldsymbol{r}})$ varies slowly over the size of an angular pixel. Then, the angular transform is performed:

$$\bar{\delta}^{\rm obs}_{n\ell m} = \sum_i \Delta\Omega_i\, Y^*_{\ell m}(\hat{\boldsymbol{r}}_i)\, \bar{\delta}^{\rm obs}_{n\ell}(\hat{\boldsymbol{r}}_i)\,. \tag{64}$$

In what follows we will generally drop the bar indicating the angular-pixel-averaging.

[1] https://healpix.jpl.nasa.gov/index.shtml
[2] https://healpy.readthedocs.io/en/latest/

D. Power spectrum estimation

Hivon *et al.* (2002), Wandelt *et al.* (2001) use a *pseudo-C_ℓ* method to estimate the power spectrum. Translating to the SFB decomposition, the pseudo-C_ℓ method assumes that much of the information about the power spectrum is contained in the pseudo-power spectrum

$$\hat{C}^{\rm obs}_{\ell nn'} = \frac{1}{2\ell+1} \sum_m \delta^{\rm obs}_{n\ell m} \delta^{{\rm obs},*}_{n'\ell m}\,. \tag{65}$$

That is, we ignore off-diagonal terms $L \neq \ell$ and $M \neq m$, and average over m. The effect of the window is then described by a mixing matrix between the $\hat{C}^{\rm obs}_{\ell nn'}$ and $\hat{C}^A_{\ell nn'}$,

$$\hat{C}^{\rm obs}_{\ell nn'} = \sum_{LNN'} \mathcal{M}^{LNN'}_{\ell nn'}\, \hat{C}^A_{LNN'}\,, \tag{66}$$

where we used Eq. (50) and defined

$$\mathcal{M}^{LNN'}_{\ell nn'} = \frac{1}{2\ell+1} \sum_{mM} W^{NLM}_{n\ell m} W^{N'LM,*}_{n'\ell m}\,, \tag{67}$$

and the index 'A' on $C^A_{\ell nn'}$ indicates the local average effect, see Section III H. Next, with Eqs. (55) and (56) we get

$$\mathcal{M}^{LNN'}_{\ell nn'} = \frac{2L+1}{4\pi} \sum_{L_1} \begin{pmatrix} \ell & L & L_1 \\ 0 & 0 & 0 \end{pmatrix}^2 \sum_{M_1} \times \int \mathrm{d}r\, r^2\, g_{n\ell}(r)\, g_{NL}(r)\, W_{L_1M_1}(r) \times \int \mathrm{d}r'\, r'^2\, g_{n'\ell}(r')\, g_{N'L}(r')\, W^*_{L_1M_1}(r')\,, \tag{68}$$

and we used the orthogonality of the Gaunt factor Eqs. (A15) and (A16). (The sum over M_1 could be performed first. However, that approach is much more memory intensive, so that computing the integrals first ends up being faster. We have also avoided expressing the result in terms of a full SFB transform, as that would require a slowly-converging sum over n.) Note that the matrix $(2L+1)^{-1}\mathcal{M}^{LNN'}_{\ell nn'}$ is symmetric, but $\mathcal{M}$ by itself is not.

1. *Separable mask and radial selection*

It is quite common that the window function is separable into a radial and an angular term,

$$W(\boldsymbol{r}) = \phi(r)\, M(\hat{\boldsymbol{r}})\,. \tag{69}$$

If the flux limit in a blind survey is near L^*, then the selection could change dramatically as a function of angular depth variations that are due to, e.g., atmospheric variations, and the separation of angular and radial selection would be a poor approximation. However, eBOSS, for

example, had more targets selected in regions where two or more plates overlapped (e.g. de Mattia *et al.* 2021). Similarly, PFS will have higher target numbers where pointings overlap (Sunayama *et al.* 2020).

When the window function is separable, then Eq. (55) is separable as well,

$$W_{LM}(r) = \phi(r)\, W_{LM}\,, \tag{70}$$

where

$$W_{LM} = \int \mathrm{d}^2\hat{\boldsymbol{r}}\, Y^*_{LM}(\hat{\boldsymbol{r}})\, M(\hat{\boldsymbol{r}})\,, \tag{71}$$

and Eq. (68) becomes

$$\begin{aligned}\mathcal{M}^{LNN'}_{\ell nn'} = \frac{2L+1}{4\pi} \sum_{L_1} \begin{pmatrix} \ell & L & L_1 \\ 0 & 0 & 0 \end{pmatrix}^2 \sum_{M_1} |W_{L_1M_1}|^2 \\ \times \int \mathrm{d}r\, r^2\, g_{n\ell}(r)\, g_{NL}(r)\, \phi(r) \\ \times \int \mathrm{d}r'\, r'^2\, g_{n'\ell}(r')\, g_{N'L}(r')\, \phi(r')\,,\end{aligned} \tag{72}$$

which is also separable, and therefore significantly reduces computation cost. Eq. (56) simplifies in a similar manner.

In the special case that $W(\boldsymbol{r}) = 1$ everywhere, we recover the unit matrix

$$\mathcal{M}^{LNN'}_{\ell nn'} = \delta^K_{\ell L}\delta^K_{nN}\delta^K_{n'N'}\,, \tag{73}$$

as expected.

E. Shot noise

The sampling of the density field by a limited number of points leads to a shot noise component in the power spectrum. To estimate the shot noise, we start with (Feldman *et al.* 1994, Peebles 1973)

$$\begin{aligned}\big\langle n(\boldsymbol{r})\, n(\boldsymbol{r}')\big\rangle &= \bar{n}(\boldsymbol{r})\, \bar{n}(\boldsymbol{r}')\, \big[1 + \xi(\boldsymbol{r},\boldsymbol{r}')\big] \\ &\quad + \bar{n}(\boldsymbol{r})\, \delta^D(\boldsymbol{r}-\boldsymbol{r}')\,, \qquad (74)\\ \big\langle n(\boldsymbol{r})\, n_r(\boldsymbol{r}')\big\rangle &= \alpha^{-1}\, \bar{n}(\boldsymbol{r})\, \bar{n}(\boldsymbol{r}')\,, \qquad (75)\\ \big\langle n_r(\boldsymbol{r})\, n_r(\boldsymbol{r}')\big\rangle &= \alpha^{-2}\, \bar{n}(\boldsymbol{r})\, \bar{n}(\boldsymbol{r}') + \alpha^{-1}\, \bar{n}(\boldsymbol{r})\, \delta^D(\boldsymbol{r}-\boldsymbol{r}')\,. \qquad (76)\end{aligned}$$

The density contrast is given by Eq. (48), and the ensemble average becomes

$$\begin{aligned}\big\langle \delta^{\mathrm{obs}}(\boldsymbol{r})\, \delta^{\mathrm{obs}}(\boldsymbol{r}')\big\rangle &= W(\boldsymbol{r})\, W(\boldsymbol{r}')\, \xi(\boldsymbol{r},\boldsymbol{r}') \\ &\quad + (1+\alpha)\, \frac{W(\boldsymbol{r})\, \delta^D(\boldsymbol{r}'-\boldsymbol{r})}{\bar{n}}\,,\end{aligned} \tag{77}$$

where we used Eq. (45). Therefore, the SFB transform of the shot noise term becomes (see Eq. (44))

$$\begin{aligned}N^{\mathrm{obs}} &= \frac{1}{\bar{n}}\, \mathrm{SFB}^2[W(\boldsymbol{r})\delta^D(\boldsymbol{r}'-\boldsymbol{r})] \qquad (78)\\ &= \frac{1}{\bar{n}}\, W^{n'\ell'm'}_{n\ell m}\,, \qquad (79)\end{aligned}$$

in the limit $\alpha \to 0$, and the W matrix is defined in Eq. (51). The window-corrected shot noise, therefore, is, in matrix form, $W^{-1}/\bar{n}$.

For the pseudo-SFB-power-spectrum estimator the shot noise simplifies significantly. Averaging over the modes $m = m'$ and assuming $\ell = \ell'$, Eq. (79) becomes

$$N^{\mathrm{obs}}_{\ell nn'} = \frac{1}{\bar{n}}\, \frac{1}{\sqrt{4\pi}} \int \mathrm{d}r\, r^2\, g_{n\ell}(r)\, g_{n'\ell}(r)\, W_{00}(r)\,, \tag{80}$$

where we used Eq. (56). Eq. (80) can be implemented very efficiently.

F. Pixel window

The pixel window refers to a distortion of the power spectrum due to binning galaxies into pixels. In the radial direction, we do not bin the galaxies, see Eq. (60), and, therefore, we do not have a radial pixel window (Leistedt *et al.* 2012).

However, the signal in Eq. (65) is still affected by the pixel window from the spherical harmonic transform. We correct this by subtracting the shot noise from the observed power spectrum, then using the `pixwin` function of `HealPy` to correct for the pixel window. We confirm the accuracy of this procedure with simulations in Section IV.

G. Bandpowers

We use a similar approach as Hivon *et al.* (2002), Alonso *et al.* (2019) to bin the SFB power spectrum into bandpowers. This is necessary as the mixing matrices in Eqs. (51) and (66) are, in general, not invertible with finite-precision arithmetic. Compared to those authors our situation is complicated, but not significantly changed, by the fact that we may need to bin not only in ℓ, but also in the k-modes n and n'.

We define the bandpower-binned pseudo-C_ℓ SFB power spectrum as a weighted sum over modes,

$$\hat{B}^{\mathrm{obs}}_{LNN'} = \sum_{\ell nn'} \widetilde{w}^{\ell nn'}_{LNN'}\, \hat{C}^{\mathrm{obs}}_{\ell nn'}\,, \tag{81}$$

where $\widetilde{w}^{\ell nn'}_{LNN'}$ is typically a rectangular sparse matrix that takes the average of neighboring modes $(\ell nn') \sim (LNN')$. The operation Eq. (81) is a type of compression, where the compression matrix $\widetilde{w}$ must satisfy the normalization

$$\sum_{\ell nn'} \widetilde{w}^{\ell nn'}_{LNN'} = 1\,. \tag{82}$$

In matrix notation, we write the compression operation Eq. (81) and the corresponding decompression operation

$$\begin{aligned} B^W &= \widetilde{w} C^W\,, & C^W &\simeq \widetilde{v} B^W\,, & (83)\\ B &= w C\,, & C &\simeq v B\,, & (84)\end{aligned}$$

where $\widetilde{w}$ and $\widetilde{v}$ are rectangular matrices operating on window-convolved power spectra, and w and v are rectangular matrices operating on cleaned power spectra. We use the index 'W' to indicate that we are only considering the window convolution. That is,

$$C^W = \mathcal{M}C\,, \qquad B^W = \mathcal{N}B\,, \tag{85}$$

where $\mathcal{M}$ is given by Eq. (67), and we can use the first of Eq. (83), the first of Eq. (85), and the last of Eq. (84) to get

$$\mathcal{N} = \widetilde{w}\mathcal{M}v\,. \tag{86}$$

The compression matrix w is obtained by inverting the second of Eq. (85), using the first of Eq. (83), and the first of Eq. (85) to get

$$B = \mathcal{N}^{-1}B^W = \mathcal{N}^{-1}\widetilde{w}C^W = \mathcal{N}^{-1}\widetilde{w}\mathcal{M}C\,, \tag{87}$$

or (Alonso *et al.* 2019),

$$w = \mathcal{N}^{-1}\widetilde{w}\mathcal{M}\,. \tag{88}$$

Similarly, we find

$$\widetilde{v} = \mathcal{M}v\mathcal{N}^{-1}\,. \tag{89}$$

Eq. (86) then implies that

$$wv = \widetilde{w}\,\widetilde{v} = I\,. \tag{90}$$

Eq. (90) is equivalent to assuming that a decompression-then-recompression cycle is lossless. That is, the compressed representation is unaffected by decompression. The opposite of compression-then-decompression, however, will in general incur losses in the compression step, so that $vw \neq I$ except in special cases.

Furthermore, once the information is lost, repeated compression-then-decompression cycles do not lose more information. That is, $(vw)^n = vw$ for integer $n \geqslant 1$.

Note that w and $\widetilde{v}$ must be calculated via Eqs. (88) and (89), because in the general case we have $(vw)^\dagger \neq vw$, and, therefore, they are not unique in satisfying Eq. (90). That is, they are not the unique Moore-Penrose inverses of the matrices v and $\widetilde{w}$ (Dresden 1920, Penrose 1955).

Since w and $\widetilde{v}$ can be expressed in terms of $\widetilde{w}$, v, and the window mixing matrix, our procedure consists of choosing a compression matrix $\widetilde{w}$ and a decompression matrix v.

How to choose $\widetilde{w}$ and v? For $\widetilde{w}$ we have already suggested that its operation on a power spectrum shall weigh neighboring modes equally and satisfy the normalization Eq. (82). Since the modes n and n' refer to modes $k_{n\ell}$, their spacing is not independent, and we need to bin four modes, nine modes, or similar at a time. In this paper, our binning strategy is completely specified by the two numbers $\Delta\ell$ and Δn.

A natural choice for the decompression v is, then, as the Moore-Penrose inverse of $\widetilde{w}$. Indeed, for the aforementioned choice for $\widetilde{w}$ that takes the average of neighboring modes, this means that v is a step function that assigns the same value or a value proportional to $\ell\,(\ell+1)$ to all modes within a bin (Hivon *et al.* 2002, Alonso *et al.* 2019).

Finally, to compare the binned power spectrum with a theoretical estimate the first of Eq. (84) must be applied to the theoretical prediction.

H. Local Average Effect

In this section we recognize that the average number density $\bar{n}$ in Eq. (48) must in practice be measured from the survey itself. This is often called the *integral constraint* (Beutler *et al.* 2014, de Mattia and Ruhlmann-Kleider 2019) or the *local average effect* (de Putter *et al.* 2012, Wadekar *et al.* 2020), and here we show that it suppresses the largest measured SFB mode in the survey.

Measuring the average number density is accomplished by dividing the total number of galaxies in the survey by the effective volume. However, the total number of galaxies in the survey is a stochastic quantity such that the average number density is given by

$$\bar{n} = \big(1+\bar{\delta}\,\big)\,\bar{n}^{\,\mathrm{true}}\,, \tag{91}$$

where $\bar{n}^{\,\mathrm{true}}$ is the underlying density contrast in the whole universe, and the average density contrast in the survey volume is

$$\bar{\delta} = \frac{1}{V_{\mathrm{eff}}}\int \mathrm{d}^3\boldsymbol{r}\,W(\boldsymbol{r})\,\delta(\boldsymbol{r})\,, \tag{92}$$

with the effective volume defined in Eq. (46). Therefore, with our model in Eq. (48), the measured density contrast is (Taruya *et al.* 2021)

$$\delta^{\mathrm{obs}}(\boldsymbol{r}) \equiv \delta^{W,A}(\boldsymbol{r}) = W(\boldsymbol{r})\,\frac{\delta(\boldsymbol{r})-\bar{\delta}}{1+\bar{\delta}}\,, \tag{93}$$

where $\delta(\boldsymbol{r})$ is the true density contrast, the superscript 'A' refers to the local average effect, and the superscript 'W' refers to the effect of the window convolution.

The SFB transform of Eq. (93) is

$$\delta^{W,A}_{n\ell m} = \sum_{n'\ell'm'} W^{n'\ell'm'}_{n\ell m}\,\frac{\delta_{n'\ell'm'} - d_{n'\ell'm'}\,\bar{\delta}}{1+\bar{\delta}}\,, \tag{94}$$

where we used Eqs. (44) and (50), and we defined

$$d_{n'\ell'm'} = \sqrt{4\pi}\,\delta^K_{\ell'0}\delta^K_{m'0}\int \mathrm{d}r\,r^2\,g_{n'0}(r)\,. \tag{95}$$

Using Eqs. (43), (44) and (50), Eq. (92) can be written

$$\bar{\delta} = \frac{1}{V_{\mathrm{eff}}}\sum_{n'\ell'm'} d^{W,*}_{n'\ell'm'}\,\delta_{n'\ell'm'}\,, \tag{96}$$

where we used Eq. (53) to define $d^W_{n'\ell'm'}$ as

$$d^W_{n'\ell'm'} = \sum_{n\ell m} W^{n\ell m}_{n'\ell'm'}\, d_{n\ell m}\,. \tag{97}$$

Then, expanding Eq. (94) for small $\bar\delta$ we get

$$\delta^{W,A}_{n\ell m} = \sum_{n'\ell'm'} W^{n'\ell'm'}_{n\ell m}\Big[\delta_{n'\ell'm'} - d_{n'\ell'm'}\,\bar\delta - \delta_{n'\ell'm'}\bar\delta + d_{n'\ell'm'}\,\bar\delta^2 + \delta_{n'\ell'm'}\bar\delta^2 + \mathcal{O}(\bar\delta^3)\Big]. \tag{98}$$

Since $d_{n\ell m}\sim\sqrt{V}$ and $\bar\delta\sim 1/\sqrt{V}$ we expand in the volume V. We also assume $C_{\ell nn'}\ll V_{\rm eff}$. Then, the correlation function becomes

$$\begin{aligned}\Big\langle \delta^{W,A}_{NLM}\,\delta^{W,A,*}_{N'L'M'}\Big\rangle &= \sum_{n\ell m} W^{n\ell m}_{NLM}\sum_{n'\ell'm'} W^{n'\ell'm',*}_{N'L'M'} \\ &\times\Big[\big\langle\delta_{n\ell m}\,\delta^*_{n'\ell'm'}\big\rangle - \big\langle\delta_{n\ell m}\,\bar\delta\big\rangle\, d_{n'\ell'm'} - d_{n\ell m}\big\langle\delta^*_{n'\ell'm'}\,\bar\delta\big\rangle \\ &+ d_{n\ell m}d_{n'\ell'm'}\big\langle\bar\delta^2\big\rangle + \mathcal{O}\Big(V^{-\frac{1}{2}}\Big)\Big],\end{aligned} \tag{99}$$

where we assume the field δ to be Gaussian. The 2-point terms entering this expression are

$$\big\langle\delta_{n\ell m}\,\delta^*_{n'\ell'm'}\big\rangle = \delta^K_{\ell\ell'}\delta^K_{mm'}\,C_{\ell nn'} + \frac{1}{\bar n}\,(W^{-1})^{n'\ell'm'}_{n\ell m}\,, \tag{100}$$

$$\big\langle\delta_{n\ell m}\,\bar\delta\big\rangle = \frac{1}{V_{\rm eff}}\sum_{n''} d^W_{n''\ell m}\,C_{\ell nn''} + \frac{1}{\bar n V_{\rm eff}}\,d_{n\ell m}\,, \tag{101}$$

$$\big\langle\bar\delta^2\big\rangle = \frac{1}{V^2_{\rm eff}}\sum_{\ell_1 n_1 n_2} D^W_{\ell_1 n_1 n_2}\,C_{\ell_1 n_1 n_2} + \frac{1}{\bar n V^2_{\rm eff}}\sum_{n_1\ell_1 m_1} d_{n_1\ell_1 m_1}\,d^W_{n_1\ell_1 m_1}\,, \tag{102}$$

where we included the shot noise term Eq. (79), and we defined the unnormalized power spectrum of a constant field

$$D^W_{\ell_1 n_1 n_2} = \sum_{m_1} d^W_{n_1\ell_1 m_1}\,d^{W,*}_{n_2\ell_1 m_1} \tag{103}$$

$$= (2\ell_1+1)\sum_{n_1'}\sum_{n_2'}\mathcal{M}^{0n_1'n_2'}_{\ell_1 n_1 n_2}\,d_{n_1'00}\,d_{n_2'00}\,, \tag{104}$$

and Eq. (67) was used in the last line. Now the correlation function becomes

$$\Big\langle\delta^A_{n\ell m}\,\delta^{A,*}_{n'\ell'm'}\Big\rangle = \delta^K_{\ell\ell'}\delta^K_{mm'}\,C_{\ell nn'} + \frac{1}{\bar n}\,(W^{-1})^{n'\ell'm'}_{n\ell m} - d_{n'\ell'm'}\frac{1}{V_{\rm eff}}\sum_{n''} d^W_{n''\ell m}\,C_{\ell nn''} - d_{n\ell m}\frac{1}{V_{\rm eff}}\sum_{n''} d^{W,*}_{n''\ell'm'}\,C_{\ell' n'n''} + \left[\frac{2}{\bar n V_{\rm eff}} + \big\langle\bar\delta^2\big\rangle\right] d_{n\ell m}\,d_{n'\ell'm'} + \mathcal{O}\Big(V^{-\frac{1}{2}}\Big)\,, \tag{105}$$

where we corrected for the window function. Only the first and fifth terms are proportional to $\delta^K_{\ell\ell'}\delta^K_{mm'}$, and so we cannot take the pseudo-$C_{\ell nn'}$ power spectrum at this stage.[3] To do so, we now add back the two window functions in Eq. (99) to get a prediction for the observed pseudo power spectrum

$$\begin{aligned}C^{W,A}_{LNN'} &= \sum_{\ell nn'}\mathcal{M}^{\ell nn'}_{LNN'}\,C_{\ell nn'} + N^{\rm obs}_{LNN'} - \frac{1}{V_{\rm eff}}\frac{1}{2L+1}\sum_M d^{W,*}_{N'LM}\sum_{n\ell m} W^{n\ell m}_{NLM}\sum_{n''} d^W_{n''\ell m}\,C_{\ell nn''} \\ &- \frac{1}{V_{\rm eff}}\frac{1}{2L+1}\sum_M d^W_{NLM}\sum_{n'\ell'm'} W^{n'\ell'm',*}_{N'LM}\sum_{n''} d^{W,*}_{n''\ell'm'}\,C_{\ell' n'n''} + \sum_{\ell nn'}\mathcal{M}^{\ell nn'}_{LNN'}\,\delta^K_{\ell 0}d_{n00}d_{n'00}\left[\frac{2}{\bar n V_{\rm eff}} + \big\langle\bar\delta^2\big\rangle\right] \\ &+ \mathcal{O}\Big(V^{-\frac{1}{2}}\Big)\,,\end{aligned} \tag{106}$$

where we used Eq. (80). The third and fourth terms are the same except for $N\leftrightarrow N'$. To simplify these two terms, we express them in terms of chains of window functions W_k that we define in Eq. (E1) and study in Appendix E. We

[3] If $d^W_{n\ell m}\propto\delta^K_{\ell 0}\delta^K_{m0}$ would be a good approximation, which is the case in the absence of a window function, then the pseudo-C_ℓ approach works well. This is an argument for using eigenfunctions tailored to the survey geometry. That is, if the window effects are already captured by the eigenfunctions, then the calculation here would simplify dramatically.

use Eq. (97) and get

$$\sum_M d^{W,*}_{N'LM} \sum_{n\ell m} W^{n\ell m}_{NLM} \sum_{n''} d^{W}_{n''\ell m}\, C_{\ell nn''} = \sum_M \sum_{n'\ell'm'} \sum_{n\ell m} \sum_{n''} \sum_{n_1\ell_1 m_1} W^{n'\ell'm',*}_{N'LM} W^{n\ell m}_{NLM} W^{n_1\ell_1 m_1}_{n''\ell m}\, d_{n'\ell'm'}\, d_{n_1\ell_1 m_1}\, C_{\ell nn''}$$
$$= \sum_{\ell nn''} \sum_{\ell' n_1 n'} \sum_{Mmm'} W^{N'LM}_{n'\ell'm'} W^{n\ell m}_{NLM} W^{n_1\ell' m'}_{n''\ell m}\, \delta^K_{\ell'0}\, d_{n'00}\, d_{n_100}\, C_{\ell nn''}$$
$$= \sum_{\ell' n_1 n'} \delta^K_{\ell'0}\, d_{n'00}\, d_{n_100} \sum_{\ell nn''} C_{\ell nn''}\, W_3 \begin{pmatrix} L & \ell & \ell' \\ N' & n & n_1 \\ N & n'' & n' \end{pmatrix}, \tag{107}$$

where W_3 is defined in Eq. (E1). Eq. (106) now becomes

$$C^{W,A}_{LNN'} = \sum_{\ell nn'} \mathcal{M}^{\ell nn'}_{LNN'} \left[C_{\ell nn'} + \delta^K_{\ell 0} d_{n00} d_{n'00} \left(\frac{2}{\bar{n} V_{\rm eff}} + \left\langle \bar{\delta}^2 \right\rangle \right) \right] + N^{\rm obs}_{LNN'}$$
$$- \frac{1}{V_{\rm eff}} \frac{1}{2L+1} \sum_{\ell' n_1 n'} \delta^K_{\ell'0}\, d_{n_100}\, d_{n'00} \sum_{\ell nn''} C_{\ell nn''} \left[W_3 \begin{pmatrix} L & \ell & \ell' \\ N' & n & n_1 \\ N & n'' & n' \end{pmatrix} + \left\langle N \leftrightarrow N' \right\rangle \right]. \tag{108}$$

The window de-convolved power spectrum is then $C^A = \mathcal{M}^{-1} C^{W,A}$.

In the absence of a window function and assuming $C_{\ell nn'} \propto \delta^K_{nn'}$, as well as using Eq. (95), we get

$$C^A_{\ell nn'} \simeq \left(1 + \frac{3A\, C_{011}}{V_{\rm eff}} \right) C_{\ell nn'} - \delta^K_{\ell 0} \frac{d_{n00}\, d_{n'00}}{V_{\rm eff}}\, B_{nn'}\,, \tag{109}$$

where we included further terms from the expansion Eq. (99), and we defined

$$A = \sum_{n_1} \frac{d^2_{n_100}}{V_{\rm eff}} \frac{C_{0n_1n_1}}{C_{011}}\,, \tag{110}$$

$$B_{nn'} = C_{0nn} + C_{0n'n'} - A\, C_{011} - \frac{6\, C_{0nn}\, C_{0n'n'}}{V_{\rm eff}}\,. \tag{111}$$

To a good approximation $A \simeq 1$, and the last term in $B_{nn'}$ can be neglected if the effective volume is sufficiently large and the shot noise sufficiently low. Furthermore, a good approximation is $d_{n00} \propto \delta^K_{n1}$. Therefore, only the $(\ell, n, n') = (0, 1, 1)$ mode is significantly affected. That is, the main effect of super-sample variance on the measured power spectrum is to reduce the power in the largest mode.

I. Covariance matrix of power spectrum

In this section we provide a covariance matrix for the SFB power spectrum. Several approaches have been used previously. Percival *et al.* (2004), Wang *et al.* (2020) trace the likelihood function either on a grid or using Markov Chain Monte Carlo techniques. Wang *et al.* (2020), e.g., use simulations to measure the covariance matrix from suites of mock catalogues. An analytical approach for the 3D power spectrum multipoles is presented in Wadekar and Scoccimarro (2020). In this paper, we get an analytical estimate for the SFB power spectrum assuming that the density contrast is Gaussian, and we compare to 100 log-normal simulations. Non-Gaussian terms in the form of the disconnected trispectrum could be included similarly to Taruya *et al.* (2021), Sugiyama *et al.* (2020).

Super-sample variance (e.g., de Putter *et al.* 2012, Lacasa and Grain 2019, Li *et al.* 2018) can have a significant impact on the covariance matrix. *Beat coupling* is mode mixing due to the window function with correlation between pairs of non-linear modes and one large mode. The *local average effect* is due to the large-scale mode modulating the average number density inside the survey volume. Both these effects can be treated in the manner of Section III H and Eq. (93).

The covariance matrix on the observed SFB power spectrum is

$$V^{LNN',\rm obs}_{\ell nn'} \equiv \left\langle \hat{C}^{\rm obs}_{\ell nn'}\, \hat{C}^{\rm obs}_{LNN'} \right\rangle - C^{\rm obs}_{\ell nn'}\, C^{\rm obs}_{LNN'}$$
$$= \frac{1}{(2\ell+1)(2L+1)} \sum_{mM} \Big[\left\langle \delta^{W,A}_{n\ell m} \delta^{W,A}_{NLM} \right\rangle \left\langle \delta^{W,A,*}_{n'\ell m} \delta^{W,A,*}_{N'LM} \right\rangle$$
$$+ \left\langle \delta^{W,A}_{n\ell m} \delta^{W,A,*}_{N'LM} \right\rangle \left\langle \delta^{W,A}_{NLM} \delta^{W,A,*}_{n'\ell m} \right\rangle \Big], \tag{112}$$

where we used Wick's theorem for a Gaussian density contrast. We simplify Eq. (112) in Appendix D. However, an analytical calculation remains computationally expensive.

To get the covariance matrix for the window-corrected power spectrum, we write the matrix equation

$$V = \mathcal{N}^{-1}\, V^{\rm obs}\, \mathcal{N}^{-1,T}\,. \tag{113}$$

where $\mathcal{N}$ is the bandpower-binned window coupling matrix given in Eq. (86), and the binning of the covariance matrix is implied.

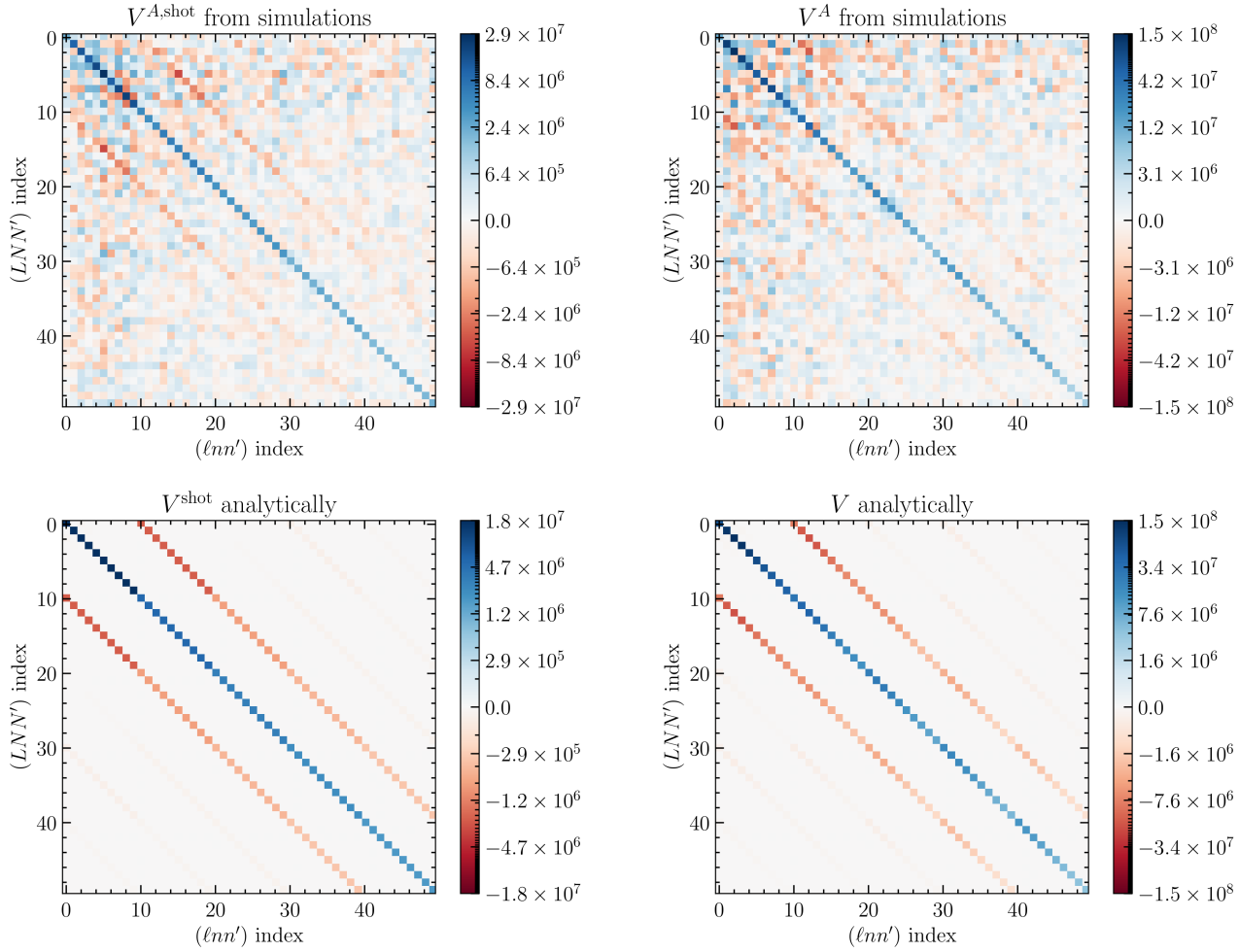

FIG. 5. The panels show the covariance matrix V defined in Eq. (113). Top row: V^A as measured from 100 simulations, including the local average effect. Bottom row: The analytical prediction, without local average effect. Left column: Shot noise only. Right column: Linear power spectrum with shot noise. Here we use a simulation with 50 % sky coverage and bandpower binning with $\Delta\ell = 2$. The order of the $(\ell nn')$ indices is such that each block of ten indices is for one ℓ-bin starting with $\ell = 0, 1$ for the block starting with index 0 and ending with $\ell = 8, 9$ for the block starting at index 40. Within each block $n = n'$ increases from one to 10. Note that the nonlinear color scheme amplifies small elements.

A reasonably precise estimate can be obtained by counting modes and assuming the covariance matrix is diagonal. That is,

$$V^{LNN'}_{\ell nn'} \simeq \frac{\delta^K_{\ell L}}{N_{\mathrm{modes}}} \left[C^{\mathrm{binned}}_{\ell nN} C^{\mathrm{binned}}_{Ln'N'} + C^{\mathrm{binned}}_{\ell nN'} C^{\mathrm{binned}}_{Ln'N} \right], \tag{114}$$

where the power spectrum includes the shot noise, $C^{\mathrm{binned}}_{\ell nn'} = C^{\mathrm{signal}}_{\ell nn'} + N^{\mathrm{shot}}_{\ell nn'}$, and

$$N_{\mathrm{modes}} = f_{\mathrm{vol}} \, (2\ell + 1) \, \Delta\ell \, \Delta n \,, \tag{115}$$

where $\Delta\ell$ and Δn are the bin widths for modes $k_{n\ell}$, and f_{vol} is the fraction of the SFB transform-volume that is occupied by the survey, defined by

$$f_{\mathrm{vol}} \equiv \frac{1}{V_{\mathrm{SFB}}} \int \mathrm{d}^3\boldsymbol{r} \, \tau[W(\boldsymbol{r}) - W_{\mathrm{threshold}}] \,, \tag{116}$$

where $\tau(x)$ is a step function and $W_{\mathrm{threshold}}$ is a threshold of the window function.

The shot noise takes into account the variation of the number density across the survey, and it enters in Eq. (114) as part of the power spectrum. The incomplete volume coverage enters as a reduction in the number of modes, and it is needed for the stability of the window-deconvolution when there are large unobserved regions in the SFB volume.

In Fig. 5 we show the covariance matrices for a set of simulations that contain only shot noise (top left) as well as for a set of simulations with a physical galaxy power spectrum with bias $b = 1.5$ at effective redshift $z_{\mathrm{eff}} = 2$ (top right). In the figure we also show the analytical result from Eq. (112) (bottom panels).

The colorbar in the figure is nonlinear. As a result, small elements appear amplified. To provide a more use-

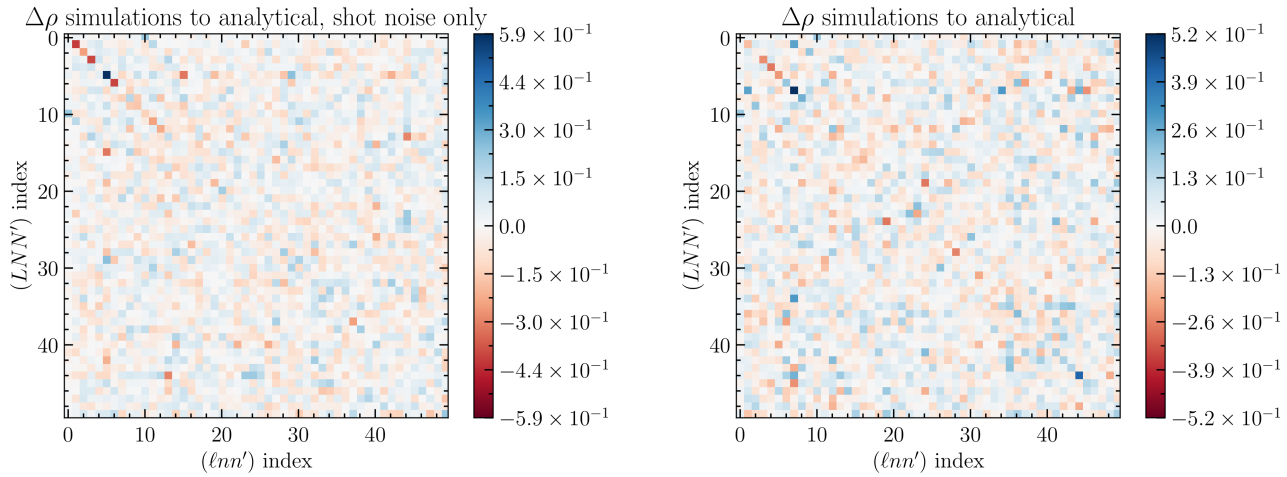

FIG. 6. Relative comparison between the covariance matrices as in Eq. (117). This avoids amplifying small deviations far from the center diagonal, and it shows that the analytic result largely agrees with the simulations. The very largest mode is set to zero, because it is affected by the local average effect that is not included in the analytical result (see Fig. 7).

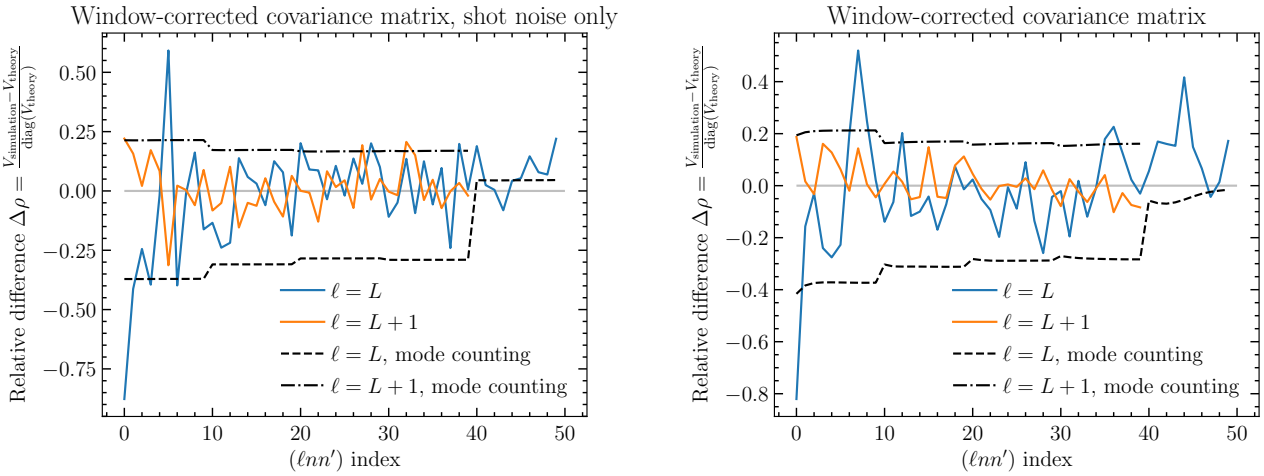

FIG. 7. Comparison of the diagonal and the $\ell = L + 1$ off-diagonal window-corrected covariance between simulations and analytical result. Left shows the shot noise only, and right including shot noise and a non-zero power spectrum. In the analytical result we do not include local average effect. Thus, the first mode in the simulations is suppressed compared to the analytical result. The black dashed and dash-dotted lines show the approximate result from mode-counting Eq. (114).

ful comparison, we introduce the difference between two covariance matrices, scaled to the center diagonal. That is, we introduce the relative difference

$$\Delta\rho_{ij} = \frac{C^A_{ij} - C^B_{ij}}{\sqrt{C^B_{ii}\, C^B_{jj}}}\,, \tag{117}$$

and we choose C^B to refer to the analytic result. $\Delta\rho$ does not suffer from amplification of small differences far from the diagonal.

Therefore, in Fig. 6 we show the relative difference between the covariance matrix as obtained from simulations and the analytical result. However, in the figure we remove the largest mode, since we have not included the local average effect in the analytical calculation. All other modes are statistically essentially equal between simulation result and analytics.

To show this more clearly, we present Fig. 7, where we compare the main diagonal and the $\ell = L + 1$ diagonal of the covariance matrices using the same statistic Eq. (117). Within the noise, we find good agreement between simulations and analytical result.

J. Performance scaling

In this section we give a brief overview of the performance behavior of the code. We consider the scaling

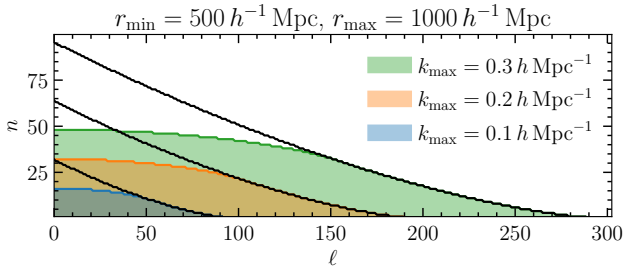

FIG. 8. Here we show the modes that are required to achieve a given $k_{\rm max}$ for the given radial boundaries. The solid black curves are constant-k contours for $r_{\rm min} = 0$.

of the SFB decomposition, the coupling matrix, and the number of modes with the parameters of the SFB power spectrum estimation.

Typically, it is desirable to calculate all modes up to some $k_{\rm max}$. The total number of modes can be estimated in the same way as for a standard Fourier transform by estimating the fundamental frequency from the volume that is being transformed, i.e., $V_{\rm SFB} \simeq \frac{4\pi}{3}\left(r_{\rm max}^3 - r_{\rm min}^3\right)$ and $k_F \simeq 2\pi/V_{\rm SFB}^{1/3}$. Then, the total number of modes is approximately $N_{\rm modes} \simeq \frac{4\pi}{3}\,k_{\rm max}^3/k_F^3 \simeq \frac{1}{18\pi}\,k_{\rm max}^3\left(r_{\rm max}^3 - r_{\rm min}^3\right)$. These are the modes that need to be calculated for transform.

However, as shown in Fig. 8, the boundary at $r_{\rm min}$ changes the structure about which modes need to be calculated. In the figure, modes with $k \leqslant k_{\rm max}$ are in the shaded region when, for illustration, $r_{\rm min} = 500\,h^{-1}\,{\rm Mpc}$, and all the modes below the solid black curves need to be calculated if $r_{\rm min} = 0$. The figure shows that fewer low-ℓ modes are needed when $r_{\rm min}$ is finite. However, most modes are at large ℓ, and, therefore, this is only a small computational reduction.

The algorithm now scales as follows. First, the sum in Eq. (60) is performed, and then for each (n,ℓ)-combination the spherical harmonic transform Eq. (64) is performed. Hence, the execution time of the transform scales as

$$T \sim \mathcal{O}\left[n_{\rm max}\,\ell_{\rm max}\left(N_{\rm gal} + N_\ell^{\rm Healpix}\right)\right], \tag{118}$$

where $N_\ell^{\rm Healpix} \sim N_{\rm pix}^{3/2}$ is the number of operations needed for the spherical harmonic transform, and $N_{\rm pix}$ is the number of HEALPix pixels.

To estimate $N_{\rm pix} = 12n_{\rm side}^2$, we need to estimate $n_{\rm side}$, which we do by considering the angular resolution. Recommended[4] is $\ell_{\rm max} \simeq 2n_{\rm side}$. However, our algorithms dealing with the window function will need to go to $L = 2\ell_{\rm max}$. Hence, we estimate

$$n_{\rm side} = 2^{{\rm ceil}\left(\log_2\left(\ell_{\rm max}+\frac{1}{2}\right)\right)}, \tag{119}$$

where ceil(x) is the smallest integer greater than x. Eq. (119) guarantees that $n_{\rm side}$ is a power of two.

The angular resolution is determined by $\ell_{\rm max}$, which is determined by $k_{\rm max}$ and $r_{\rm max}$ by Limber's relation Eq. (36). However, we note that the actual number needed for $\ell_{\rm max}$ tends to be smaller by a few percent.

IV. FUTURE APPLICATIONS

In this section we will test the SFB estimator presented in this paper for several use cases. First, we will consider simplistic simulations of surveys similar to the High-Latitude Spectroscopic Survey (HLSS) of the *Nancy Grace Roman Space Telescope* which will benefit from large radial modes, and we will consider *SPHEREx* and *Euclid* for wide-angle surveys.

We bin into bandpowers by selecting

$$\Delta\ell \simeq \frac{1}{f_{\rm sky}}\,, \tag{120}$$

and then we round to the nearest integer. Eq. (115) then suggests

$$\Delta n \simeq \frac{f_{\rm sky}}{f_{\rm vol}}\,. \tag{121}$$

For all cases in this paper, this results in $\Delta n = 1$.

To do the window deconvolution, it is important to ensure that all modes are complete. For the angular power spectrum, Alonso *et al.* (2019), Leistedt *et al.* (2013) suggest estimating up to $2\ell_{\rm max}$, and then discarding all the modes above $\ell_{\rm max}$. Wang *et al.* (2020) argue that (in our notation) the sum Eq. (66) only converges with the inclusion of modes $k_{n\ell} > k_{\rm max}$, and they do numerical experiments to estimate the maximum k needed.

We take a similar approach, which is demonstrated in Fig. 9, where in the left panel the relative contribution of window-convolved modes to a physical mode near $k_{\rm max}$ is shown. That is, we plot the relative contributions of all observed modes $(\ell nn')$ that contribute to the physical mode (LNN') using Eq. (66). Assuming a flat power spectrum and summing the absolute values of the coupling matrix $\mathcal{M}^{-1}$, then, allows us to estimate the contribution from all modes above some $k_{\rm large}$. This is shown in the right panel of Fig. 9.

Next, we iteratively increase $k_{\rm large}$ until the contribution from $k_{n\ell} > k_{\rm large}$ to the most affected mode $k_{NL} \leqslant k_{\rm max}$ is less than 1 %. The results for $k_{\rm large}$ are the dashed vertical lines in either panel of Fig. 9.

That is, by including all modes up to $k_{\rm large} > k_{\rm max}$ in the SFB power spectrum estimation, we get reasonable confidence that all modes $k < k_{\rm max}$ can be fully deconvolved by the inversion of Eq. (66).

[4] https://healpix.jpl.nasa.gov/

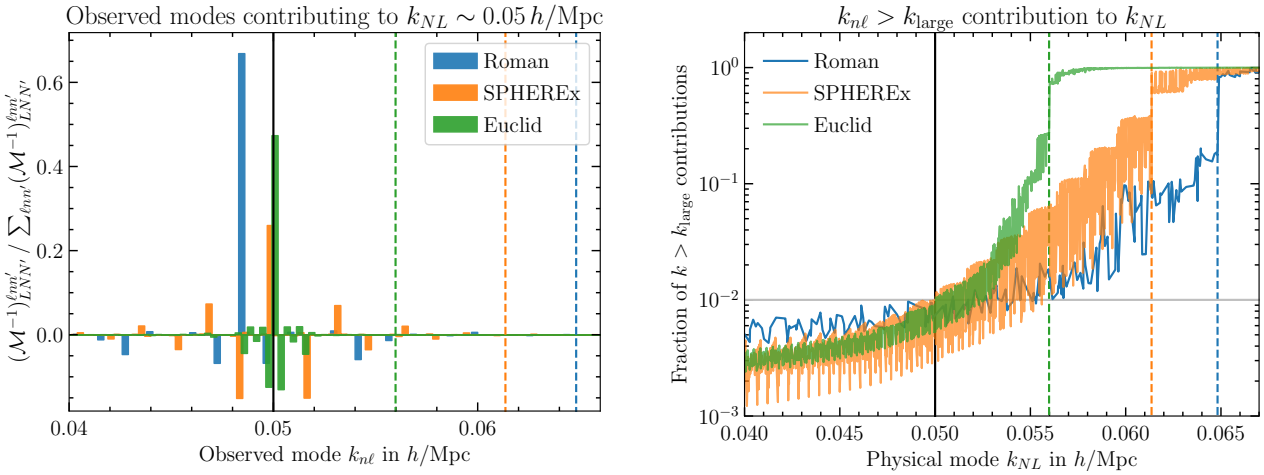

FIG. 9. This figure shows the relative contributions from hi-k observed (window-convolved) modes to physical modes close to $k_{\mathrm{max}} = 0.05\,h\,\mathrm{Mpc}^{-1}$ (vertical black line). The left panel shows a histogram of the contributions to a single physical mode. Since there are modes above k_{max} that are contributing in the deconvolution of the window (the inversion of Eq. (66)) we include all the modes up to the dashed lines at k_{large}, which are colored by survey. The specific physical mode chosen is the one that has the most contribution from modes above k_{large} (the dashed line), and the dashed lines are chosen so that their cumulative contribution is less than 1 %. The right panel shows the cumulative contribution from observed modes $k > k_{\mathrm{large}}$ for each physical mode k_{NL}. The vertical lines are the same as in the left plot, the horizontal line marks our target maximum contribution of 1 %.

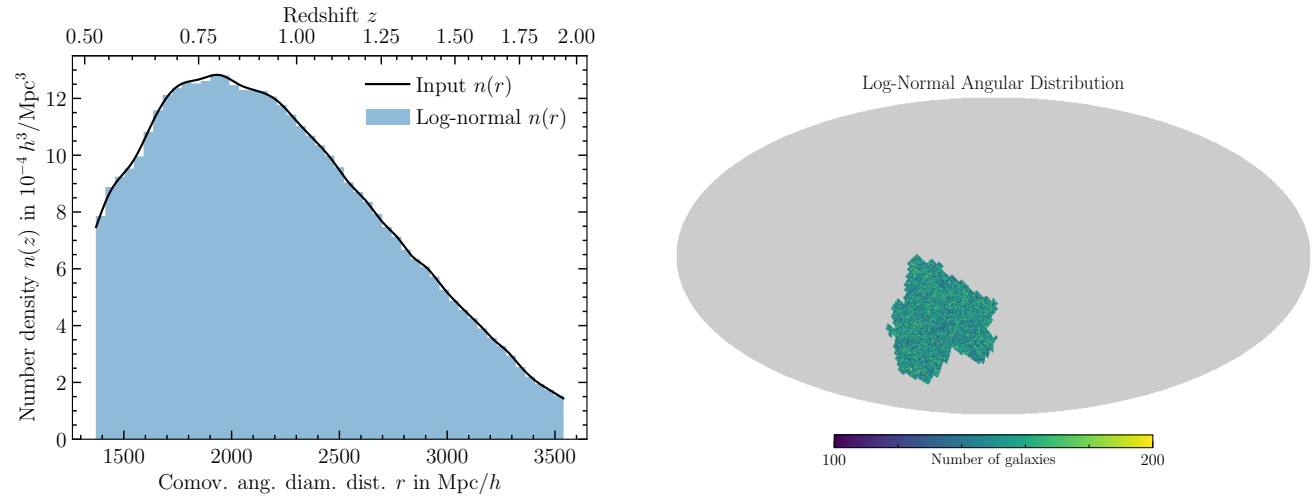

FIG. 10. The plots show the approximate Roman radial selection function and angular mask. In addition one realization of a log-normal simulation is shown.

A. Roman

In this section we apply the SFB power spectrum estimator to a log-normal simulation for the High-Latitude Spectroscopy Survey (HLSS) of the *Nancy Grace Roman Space Telescope* (Spergel *et al.* 2015). The notional survey area is currently planned as ∼6 % of the sky. Our main objective here, however, is to exploit the large radial selection that *Roman* will provide.

The grism spectroscopy of the HLSS will yield observed wavelengths 1 µm to 1.93 µm[5], which for the Hα line at 6562.8 Å results in a redshift range $0.523 \leqslant z \leqslant 1.94$, and for the simulations we round this to the range $1370\,h^{-1}$ Mpc to $3540\,h^{-1}$ Mpc. The radial selection for our simulation is shown in the left panel of Fig. 10 (Eifler *et al.* 2020).

The right panel of Fig. 10 shows the HEALPix projec-

[5] https://roman.ipac.caltech.edu/sims/Param_db.html#wfi_grism

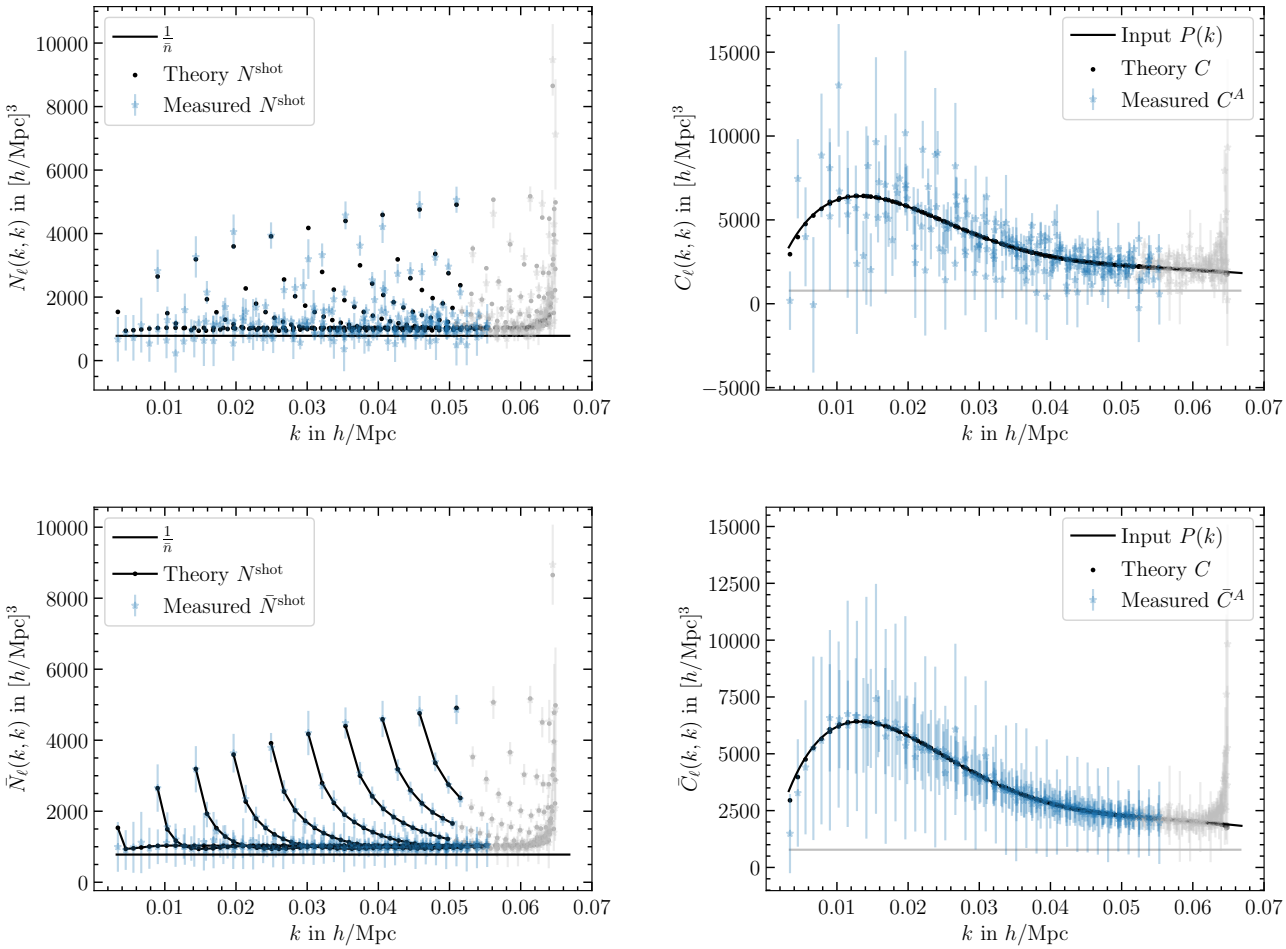

FIG. 11. SFB power spectrum measurement from uniform shot-noise-only (left column) and log-normal (right column) simulations with Roman window function. The top row is for a single simulation, the bottom shows the average over 50 simulations. In each panel, the grey-painted modes near $k_{\rm max}$ are incomplete bandpower bins, and we show them for illustration only. On the right panels, the theory points take into account the bandpower binning with $\Delta\ell = 18$. The horizontal line in each plot is $\frac{1}{\bar{n}}$. The local average effect suppresses the largest-scale mode in the simulations. Note that here we only estimate the Hα sample of *Roman*.

tion of our log-normal simulation (Agrawal *et al.* 2017), where we use an approximate binary Roman mask. The window function is then constructed as the multiplication of the radial selection and mask, normalized so that the maximum is unity.

Our log-normal simulation assumes a non-evolving linear power spectrum at redshift 1.5 and linear galaxy bias $b = 1.5$. The number of galaxies is $\sim 6.6 \times 10^6$. We use a flat ΛCDM Planck cosmology.

The results of the SFB analysis are shown in Fig. 11. The top left panel shows the shot noise from a simulation with vanishing power spectrum as well as the theoretical shot noise prediction from Eq. (80). The bottom left shows the average over 50 simulations.

For a simulation with signal, we show the SFB measurement from our log-normal simulation in the top right of Fig. 11. Here, we have subtracted the theoretical shot noise. The theory points and the input $P(k)$ differ due to application of Eq. (88) to account for the bandpower binning with $\Delta\ell = 18$. The bottom right panel shows the same as an average over our ensemble of simulations.

We get good agreement between the ensemble measurement and theory power spectra if we restrict ourselves to the blue modes in Fig. 11. The greyed-out modes cannot be fully deconvolved due to the possibility of high-k contributions, as explained at the beginning of Section IV. Clearly, our estimations there were conservative, because high-k contributions vary in sign and can cancel each other.

The black curves in the lower left panel of Fig. 11 connect theory points with the same ℓ. For a given ℓ, then, the limber ratio Eq. (36) suggests that higher k corresponds to lower redshift. Since the number density tends to be higher at lower redshift, we expect the shot noise

to decrease with k given constant ℓ. This effect is much more pronounced for *SPHEREx* below.

B. SPHEREx

In this section we aim to show the feasibility of applying our estimator to *SPHEREx*[6] (Doré *et al.* 2014).

For the radial selection, we use the *SPHEREx* public products[7], and for demonstration we limit ourselves to the range $0 \leqslant r \leqslant 2000\,h^{-1}\,\mathrm{Mpc}$, corresponding to a maximum redshift of 0.83. We impose this limit due to our current lack of a large number of better simulations. The radial selection is shown in Fig. 12. *SPHEREx* is able to go down to essentially $z = 0$ since it is not limited by the detection of a single emission line but measures galaxy redshifts with 102 narrow photometric bands.

For the mask we use the HFI GAL080 mask with no apodization from the *Planck* Collaboration[8]. This cuts out the galactic plane, as shown in Fig. 12. The binning strategy in Eqs. (120) and (121) yields no binning, or $\Delta\ell = \Delta n = 1$.

Since our log-normal simulations do not take into account redshift-evolution effects, we choose a fixed effective redshift $z_{\mathrm{eff}} = 0.5$ and galaxy bias $b = 1.5$.

The estimation of the SFB shot noise and power spectrum is shown in Fig. 13. The "dotted curves" of the theory shot noise that rise quickly and then settle on an approximately constant value are curves of constant n, and each dot along a curve signifies the increase of ℓ by one. That is, lines of constant ℓ start on the first of these curves, and then decrease rapidly, as expected from the Limber ratio Eq. (36) in conjuction with a high number density at low redshifts.

Fig. 13 shows that we get good agreement between our measured SFB power spectrum with the theory power spectrum. It is only in the greyed-out modes that are not fully deconvolved that a spurious oscillatory pattern is introduced, and measuring those modes accurately is simply a matter of increasing k_{large}.

Furthermore, since in this paper we are primarily interested in testing the SFB estimator, Fig. 13 shows every mode by itself. A more intuitive visualization of the constraining power of the survey should bin the information from neighboring modes, and this would bring the error bars down significantly. We leave such visualization to a future paper. For now, every mode for itself!

[6] http://spherex.caltech.edu
[7] https://github.com/SPHEREx/Public-products
[8] https://irsa.ipac.caltech.edu/data/Planck/release_2/ancillary-data/previews/HFI_Mask_GalPlane-apo0_2048_R2.00/index.html

C. Euclid

As a final test for a realistic mask and selection, in this section we apply the SFB estimator to make a forecast for the spectroscopic survey of *Euclid*, which is an all-sky mission that covers approximately 40 % of the sky. For the number density, we adopt the reference case given in Amendola *et al.* (2018). We use the radial range $1645 \leqslant \frac{r}{h^{-1}\,\mathrm{Mpc}} \leqslant 3650$, shown in Fig. 14. Also shown in the figure is the mask that cuts the galactic and ecliptic planes (Markovič 2020).

Our simulation results are shown in Fig. 15, for both shot noise-only and with a power spectrum signal with and galaxy bias $b = 1.6$.

As for the other surveys, once we ignore the modes that are not fully deconvolved, we get good agreement for both cases.

V. CONCLUSION

In this paper we present a new pseudo-SFB power spectrum estimator, *SuperFaB*. The estimator analytically accounts for shot noise, mask, and selection effects. We also investigate the impact of the local average effect and the covariance matrix.

SuperFaB works by performing the radial transform before the angular transform, similar to Leistedt *et al.* (2012). In the radial direction the galaxies are treated as point-particles so that no radial pixel window needs correction. The angular transform is performed using HEALPix (Górski *et al.* 2005, Zonca *et al.* 2019).

Furthermore, we derive the radial eigenmodes with potential boundary conditions at r_{min} and r_{max}, as suggested by Samushia (2019). The boundary at $r_{\mathrm{min}} \neq 0$ eliminates the need for bandpower-binning in the radial direction, the boundary at r_{max} discretizes the measured modes $k_{n\ell}$ for integer n and ℓ.

We demonstrate that *SuperFaB* will be able to analyze all large-scale modes of upcoming wide and deep galaxy surveys such as *Roman*, *SPHEREx*, and *Euclid*.

We also review the SFB power spectrum theory and provide intuition using the Limber approximation. Notably, redshift-dependence of the power spectrum and bias factors primarily enter as the interplay between k and ℓ modes, such that $r \sim (\ell + 0.5)/k$ is an approximation for the angular diameter distance. We leave a more detailed analysis for the projection of the 3D power spectrum to SFB space and the connection with cosmological parameters for a future paper.

We also leave for a future paper the extension of the estimator to cross-correlations between samples with differing selection functions.

Since the SFB power spectrum is uniquely suited for all-sky surveys, we expect a particularly intriguing application of *SuperFaB* will be intensity mapping at high redshift, and we look forward to this possibility.

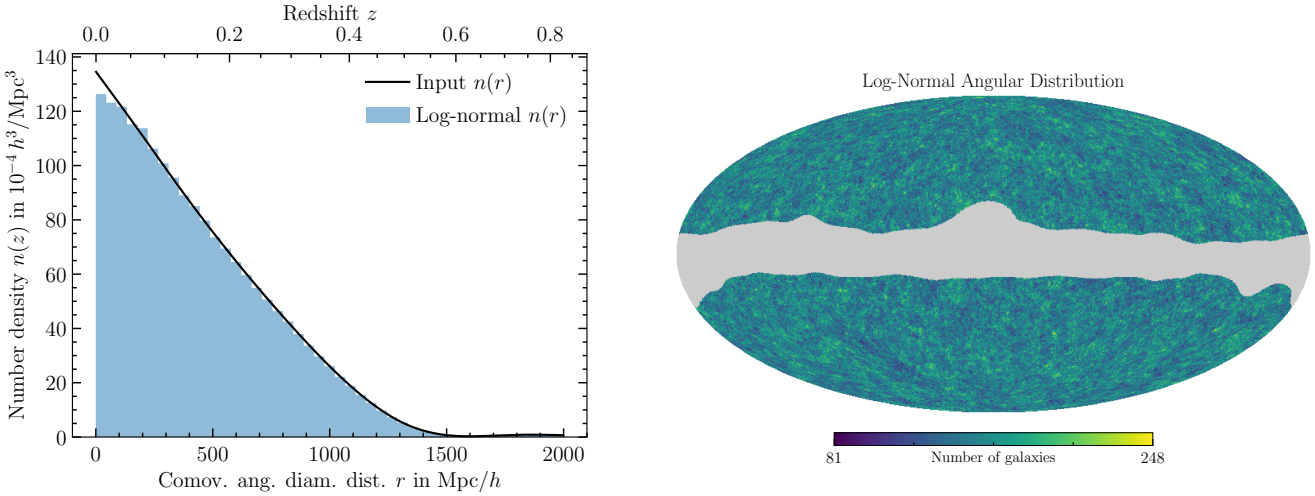

FIG. 12. The plots show the approximate radial selection function and angular mask for our *SPHEREx*-like survey.

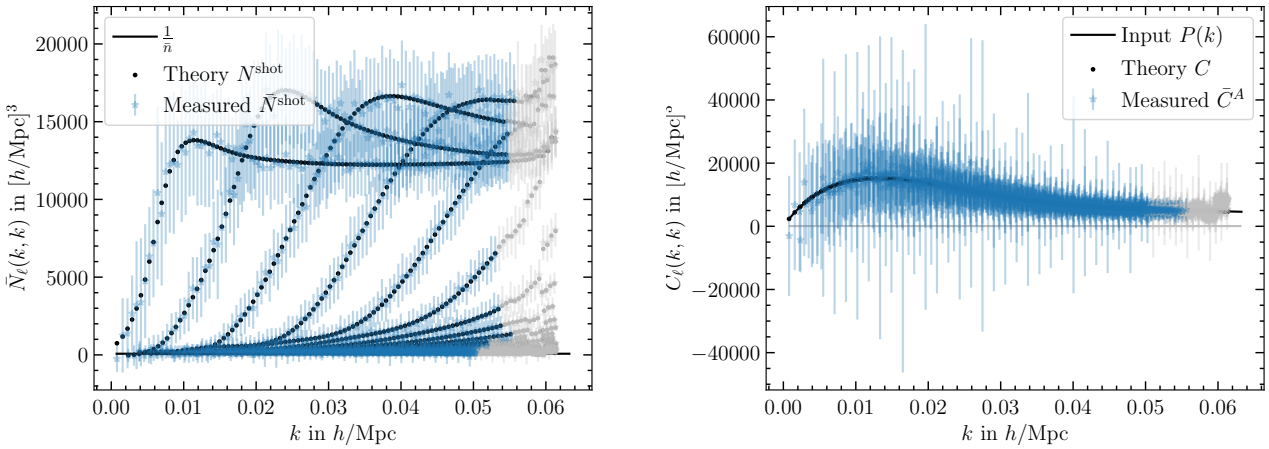

FIG. 13. The plot on the left shows the shot noise and the plot on the right the SFB power spectrum similar to Fig. 11, but now for a full-sky mission like *SPHEREx*, averaged over 50 simulations. Note that while the mask and selection are realistic, we only consider a small part of the full *SPHEREx* volume due to limitations of our mocks.

For surveys covering a compact area on the sky we can introduce boundary conditions to the angular basis functions as well, as pointed out by Samushia (2019). This would significantly reduce the size of the computational problem in these cases.

ACKNOWLEDGMENTS

 The authors thank Katarina Markovič, Christopher Hirata, Lado Samushia, Chen Heinrich, and the Nancy Grace Roman Telescope *Cosmology with the High Latitude Survey* Science Investigation Team (SIT) for discussions and providing selection functions and masks. Part of this work was done at Jet Propulsion Laboratory, California Institute of Technology, under a contract with the National Aeronautics and Space Administration. This work was supported by NASA grant 15-WFIRST15-0008 *Cosmology with the High Latitude Survey* Roman Science Investigation Team (SIT). Henry S. G. Gebhardt's research was supported by an appointment to the NASA Postdoctoral Program at the Jet Propulsion Laboratory, administered by Universities Space Research Association under contract with NASA.

D. Spergel, N. Gehrels, C. Baltay, D. Bennett, J. Breckinridge, M. Donahue, A. Dressler, B. S. Gaudi, T. Greene, O. Guyon, *et al.*, arXiv e-prints , arXiv:1503.03757 (2015),

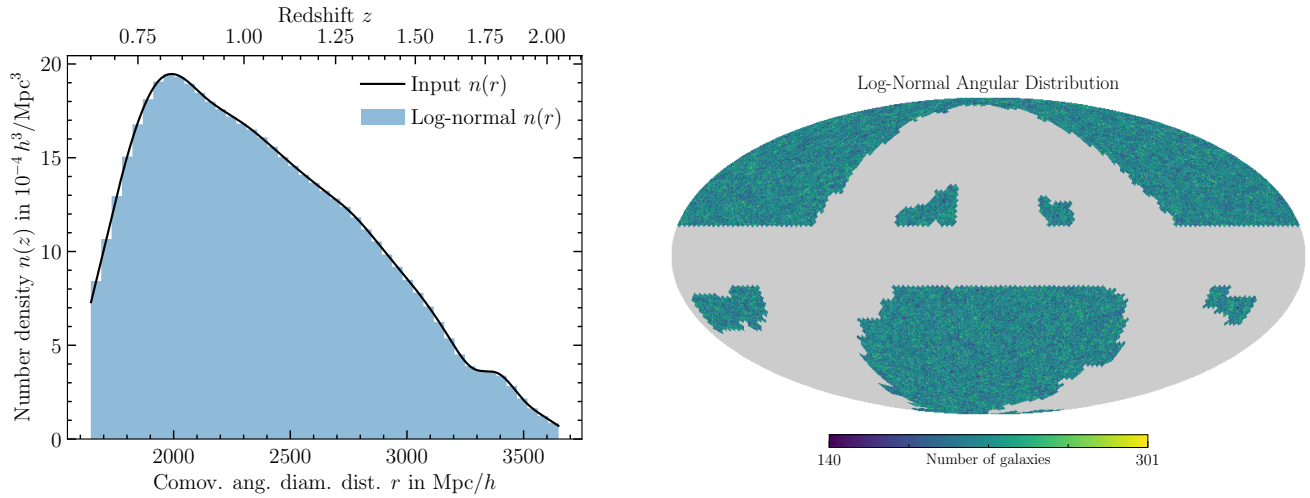

FIG. 14. The plots show the approximate radial selection function and angular mask for *Euclid* with one log-normal simulation.

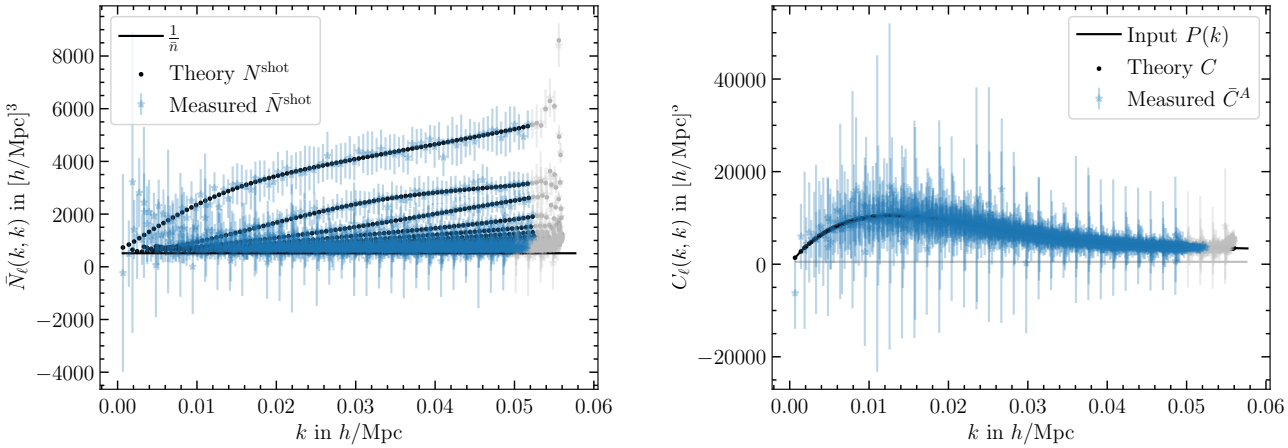

FIG. 15. The plot on the left shows the shot noise and the plot on the right the SFB power spectrum similar to Fig. 11, but now for a full-sky mission like *Euclid*, averaged over 20 simulations.

arXiv:1503.03757 [astro-ph.IM].

O. Doré, J. Bock, M. Ashby, P. Capak, A. Cooray, R. de Putter, T. Eifler, N. Flagey, Y. Gong, S. Habib, *et al.*, arXiv e-prints , arXiv:1412.4872 (2014), arXiv:1412.4872 [astro-ph.CO].

L. Amendola, S. Appleby, A. Avgoustidis, D. Bacon, T. Baker, M. Baldi, N. Bartolo, A. Blanchard, C. Bonvin, S. Borgani, *et al.*, Living Reviews in Relativity **21**, 2 (2018), arXiv:1606.00180 [astro-ph.CO].

DESI Collaboration, A. Aghamousa, J. Aguilar, S. Ahlen, S. Alam, L. E. Allen, C. Allende Prieto, J. Annis, S. Bailey, C. Balland, *et al.*, arXiv e-prints , arXiv:1611.00036 (2016), arXiv:1611.00036 [astro-ph.IM].

M. Takada, R. S. Ellis, M. Chiba, J. E. Greene, H. Aihara, N. Arimoto, K. Bundy, J. Cohen, O. Doré, G. Graves, *et al.*, PASJ **66**, R1 (2014), arXiv:1206.0737 [astro-ph.CO].

D. Munshi, G. Pratten, P. Valageas, P. Coles, and P. Brax, MNRAS **456**, 1627 (2016), arXiv:1508.00583 [astro-ph.CO].

D. S. Salopek and J. R. Bond, Phys. Rev. D **42**, 3936 (1990).

E. Komatsu and D. N. Spergel, Phys. Rev. D **63**, 063002 (2001), arXiv:astro-ph/0005036 [astro-ph].

N. Dalal, O. Doré, D. Huterer, and A. Shirokov, Phys. Rev. D **77**, 123514 (2008), arXiv:0710.4560 [astro-ph].

V. Desjacques, D. Jeong, and F. Schmidt, Phys. Rep. **733**, 1 (2018), arXiv:1611.09787 [astro-ph.CO].

K. Yamamoto, M. Nakamichi, A. Kamino, B. A. Bassett, and H. Nishioka, PASJ **58**, 93 (2006), arXiv:astro-ph/0505115 [astro-ph].

D. Bianchi, H. Gil-Marín, R. Ruggeri, and W. J. Percival, MNRAS **453**, L11 (2015), arXiv:1505.05341 [astro-ph.CO].

R. Scoccimarro, Phys. Rev. D **92**, 083532 (2015), arXiv:1506.02729 [astro-ph.CO].

F. Beutler, H.-J. Seo, A. J. Ross, P. McDonald, S. Saito, A. S. Bolton, J. R. Brownstein, C.-H. Chuang, A. J. Cuesta, D. J. Eisenstein, *et al.*, MNRAS **464**, 3409 (2017), arXiv:1607.03149 [astro-ph.CO].

G. Pratten and D. Munshi, MNRAS **436**, 3792 (2013), arXiv:1301.3673 [astro-ph.CO].

P. Reimberg, F. Bernardeau, and C. Pitrou, J. Cosmology Astropart. Phys. **2016**, 048 (2016), arXiv:1506.06596 [astro-ph.CO].

J. Binney and T. Quinn, MNRAS **249**, 678 (1991).

O. Lahav, in *Cosmic Velocity Fields*, Vol. 9, edited by F. Bouchet and M. Lachieze-Rey (1993) p. 205, arXiv:astro-ph/9309030 [astro-ph].

A. F. Heavens and A. N. Taylor, MNRAS **275**, 483 (1995), arXiv:astro-ph/9409027 [astro-ph].

H. Tadros, W. E. Ballinger, A. N. Taylor, A. F. Heavens, G. Efstathiou, W. Saunders, C. S. Frenk, O. Keeble, R. McMahon, S. J. Maddox, *et al.*, MNRAS **305**, 527 (1999), arXiv:astro-ph/9901351 [astro-ph].

W. J. Percival, D. Burkey, A. Heavens, A. Taylor, S. Cole, J. A. Peacock, C. M. Baugh, J. Bland-Hawthorn, T. Bridges, R. Cannon, *et al.*, MNRAS **353**, 1201 (2004), arXiv:astro-ph/0406513 [astro-ph].

B. Leistedt, A. Rassat, A. Réfrégier, and J. L. Starck, A&A **540**, A60 (2012), arXiv:1111.3591 [astro-ph.CO].

M. S. Wang, S. Avila, D. Bianchi, R. Crittenden, and W. J. Percival, J. Cosmology Astropart. Phys. **2020**, 022 (2020), arXiv:2007.14962 [astro-ph.CO].

L. Samushia, arXiv e-prints , arXiv:1906.05866 (2019), arXiv:1906.05866 [astro-ph.CO].

K. M. Górski, E. Hivon, A. J. Banday, B. D. Wandelt, F. K. Hansen, M. Reinecke, and M. Bartelmann, ApJ **622**, 759 (2005), arXiv:astro-ph/0409513 [astro-ph].

A. Zonca, L. Singer, D. Lenz, M. Reinecke, C. Rosset, E. Hivon, and K. Gorski, The Journal of Open Source Software **4**, 1298 (2019).

E. Hivon, K. M. Górski, C. B. Netterfield, B. P. Crill, S. Prunet, and F. Hansen, ApJ **567**, 2 (2002), arXiv:astro-ph/0105302 [astro-ph].

D. Alonso, J. Sanchez, A. Slosar, and LSST Dark Energy Science Collaboration, MNRAS **484**, 4127 (2019), arXiv:1809.09603 [astro-ph.CO].

S. Camera, J. Fonseca, R. Maartens, and M. G. Santos, MNRAS **481**, 1251 (2018), arXiv:1803.10773 [astro-ph.CO].

A. Nicola, A. Refregier, A. Amara, and A. Paranjape, Phys. Rev. D **90**, 063515 (2014), arXiv:1405.3660 [astro-ph.CO].

F. Lanusse, A. Rassat, and J. L. Starck, A&A **578**, A10 (2015), arXiv:1406.5989 [astro-ph.CO].

E. Castorina and M. White, MNRAS **476**, 4403 (2018), arXiv:1709.09730 [astro-ph.CO].

F. Beutler, E. Castorina, and P. Zhang, J. Cosmology Astropart. Phys. **2019**, 040 (2019), arXiv:1810.05051 [astro-ph.CO].

H. S. Grasshorn Gebhardt and D. Jeong, Phys. Rev. D **102**, 083521 (2020), arXiv:2008.08706 [astro-ph.CO].

M. LoVerde and N. Afshordi, Phys. Rev. D **78**, 123506 (2008), arXiv:0809.5112 [astro-ph].

F. Bernardeau, S. Colombi, E. Gaztañaga, and R. Scoccimarro, Phys. Rep. **367**, 1 (2002), arXiv:astro-ph/0112551 [astro-ph].

K. B. Fisher, O. Lahav, Y. Hoffman, D. Lynden-Bell, and S. Zaroubi, MNRAS **272**, 885 (1995), arXiv:astro-ph/9406009 [astro-ph].

A. Taruya, T. Nishimichi, and D. Jeong, Phys. Rev. D **103**, 023501 (2021), arXiv:2007.05504 [astro-ph.CO].

H. A. Feldman, N. Kaiser, and J. A. Peacock, ApJ **426**, 23 (1994), arXiv:astro-ph/9304022 [astro-ph].

B. D. Wandelt, E. Hivon, and K. M. Górski, Phys. Rev. D **64**, 083003 (2001), arXiv:astro-ph/0008111 [astro-ph].

A. de Mattia, V. Ruhlmann-Kleider, A. Raichoor, A. J. Ross, A. Tamone, C. Zhao, S. Alam, S. Avila, E. Burtin, J. Bautista, *et al.*, MNRAS **501**, 5616 (2021), arXiv:2007.09008 [astro-ph.CO].

T. Sunayama, M. Takada, M. Reinecke, R. Makiya, T. Nishimichi, E. Komatsu, S. Saito, N. Tamura, and K. Yabe, J. Cosmology Astropart. Phys. **2020**, 057 (2020), arXiv:1912.06583 [astro-ph.CO].

P. J. E. Peebles, ApJ **185**, 413 (1973).

A. Dresden, Science **52**, 393 (1920).

R. Penrose, Proceedings of the Cambridge Philosophical Society **51**, 406 (1955).

F. Beutler, S. Saito, H.-J. Seo, J. Brinkmann, K. S. Dawson, D. J. Eisenstein, A. Font-Ribera, S. Ho, C. K. McBride, F. Montesano, *et al.*, MNRAS **443**, 1065 (2014), arXiv:1312.4611 [astro-ph.CO].

A. de Mattia and V. Ruhlmann-Kleider, J. Cosmology Astropart. Phys. **2019**, 036 (2019), arXiv:1904.08851 [astro-ph.CO].

R. de Putter, C. Wagner, O. Mena, L. Verde, and W. J. Percival, J. Cosmology Astropart. Phys. **2012**, 019 (2012), arXiv:1111.6596 [astro-ph.CO].

D. Wadekar, M. M. Ivanov, and R. Scoccimarro, Phys. Rev. D **102**, 123521 (2020), arXiv:2009.00622 [astro-ph.CO].

D. Wadekar and R. Scoccimarro, Phys. Rev. D **102**, 123517 (2020), arXiv:1910.02914 [astro-ph.CO].

N. S. Sugiyama, S. Saito, F. Beutler, and H.-J. Seo, MNRAS **497**, 1684 (2020), arXiv:1908.06234 [astro-ph.CO].

F. Lacasa and J. Grain, A&A **624**, A61 (2019), arXiv:1809.05437 [astro-ph.CO].

Y. Li, M. Schmittfull, and U. Seljak, J. Cosmology Astropart. Phys. **2018**, 022 (2018), arXiv:1711.00018 [astro-ph.CO].

B. Leistedt, H. V. Peiris, D. J. Mortlock, A. Benoit-Lévy, and A. Pontzen, MNRAS **435**, 1857 (2013), arXiv:1306.0005 [astro-ph.CO].

T. Eifler, H. Miyatake, E. Krause, C. Heinrich, V. Miranda, C. Hirata, J. Xu, S. Hemmati, M. Simet, P. Capak, *et al.*, arXiv e-prints , arXiv:2004.05271 (2020), arXiv:2004.05271 [astro-ph.CO].

A. Agrawal, R. Makiya, C.-T. Chiang, D. Jeong, S. Saito, and E. Komatsu, J. Cosmology Astropart. Phys. **2017**, 003 (2017), arXiv:1706.09195 [astro-ph.CO].

K. Markovič, personal communication, paper in prep (2020).
D. N. Limber, ApJ **119**, 655 (1954).

Appendix A: Useful formulae

For any function $f(\boldsymbol{k})$

$$\int k^2 \mathrm{d}k\, \mathrm{d}^2\hat{\boldsymbol{k}}\, \delta^D(\boldsymbol{k}-\boldsymbol{k}')\, f(\boldsymbol{k}) = \int \mathrm{d}k\, \delta^D(k-k') \int \mathrm{d}^2\hat{\boldsymbol{k}}\, \delta^D(\hat{\boldsymbol{k}}-\hat{\boldsymbol{k}}')\, f(\boldsymbol{k})\,. \tag{A1}$$

Therefore,

$$\delta^D(\boldsymbol{k}-\boldsymbol{k}') = k^{-2}\, \delta^D(k-k')\, \delta^D(\hat{\boldsymbol{k}}-\hat{\boldsymbol{k}}')\,. \tag{A2}$$

Furthermore,

$$\frac{1}{r}\, \delta^D\!\left(\frac{1}{r}-\frac{1}{r_0}\right) = r\, \delta^D(r-r_0)\,. \tag{A3}$$

The first-order result from LoVerde and Afshordi (2008) can be written as

$$J_\nu(kr) \simeq \delta^D(kr-\nu)\,, \tag{A4}$$

where $J_\nu(x)$ is the Bessel function. Therefore, for a spherical Bessel function $j_\ell(x) = \sqrt{\pi/2x}\, J_{\ell+\frac{1}{2}}(x)$ we get

$$j_\ell(kr) \simeq \sqrt{\frac{\pi}{2rk}}\, \frac{1}{k}\, \delta^D\!\left(r-\frac{\ell+\frac{1}{2}}{k}\right) \tag{A5}$$

to first order. This is called *Limber's approximation* (Limber 1954).

Spherical Bessel functions and spherical harmonics satisfy orthogonality relations

$$\delta^D(k-k') = \frac{2kk'}{\pi} \int_0^\infty \mathrm{d}r\, r^2\, j_\ell(kr)\, j_\ell(k'r)\,, \tag{A6}$$

$$\delta^K_{\ell\ell'}\delta^K_{mm'} = \int \mathrm{d}\Omega_{\hat{\boldsymbol{r}}}\, Y_{\ell m}(\hat{\boldsymbol{r}})\, Y^*_{\ell' m'}(\hat{\boldsymbol{r}})\,. \tag{A7}$$

Spherical harmonics can be expressed in terms of a complex exponential and real associated Legendre functions $\mathrm{P}^m_\ell(x)$ as

$$Y_{\ell m}(\hat{\boldsymbol{r}}) = e^{im\phi} \left(\frac{(\ell-m)!(2\ell+1)}{4\pi\,(\ell+m)!}\right)^{\frac{1}{2}} \mathrm{P}^m_\ell(\cos\theta)\,. \tag{A8}$$

The completeness relation is

$$\sum_{\ell m} Y_{\ell m}(\hat{\boldsymbol{r}})\, Y^*_{\ell m}(\hat{\boldsymbol{r}}') = \delta^D(\hat{\boldsymbol{r}}-\hat{\boldsymbol{r}}')\,. \tag{A9}$$

Rayleigh's formula decomposes the plane waves into spherical Bessels and spherical harmonics,

$$e^{i\boldsymbol{q}\cdot\boldsymbol{r}} = 4\pi \sum_{\ell' m'} i^{\ell'}\, j_{\ell'}(qr)\, Y^*_{\ell' m'}(\hat{\boldsymbol{q}})\, Y_{\ell' m'}(\hat{\boldsymbol{r}})\,. \tag{A10}$$

Legendre polynomials can be expressed as a sum over spherical harmonics as

$$\mathcal{P}_\ell(\hat{\boldsymbol{k}}\cdot\hat{\boldsymbol{r}}) = \frac{4\pi}{2\ell+1} \sum_m Y_{\ell m}(\hat{\boldsymbol{k}})\, Y^*_{\ell m}(\hat{\boldsymbol{r}})\,. \tag{A11}$$

Flipping the sign of the component angular momentum or the direction of the argument to spherical harmonics gives

$$Y^*_{\ell m}(\hat{\boldsymbol{r}}) = (-1)^m Y_{\ell,-m}(\hat{\boldsymbol{r}})\,, \tag{A12}$$

$$Y_{\ell m}(-\hat{\boldsymbol{r}}) = (-1)^\ell Y_{\ell,m}(\hat{\boldsymbol{r}})\,. \tag{A13}$$

The Gaunt factor is

$$\mathcal{G}^{\ell L L_1}_{mMM_1} = \int \mathrm{d}^2\hat{\boldsymbol{r}}\, Y_{\ell m}(\hat{\boldsymbol{r}})\, Y_{LM}(\hat{\boldsymbol{r}})\, Y_{L_1 M_1}(\hat{\boldsymbol{r}})\,, \tag{A14}$$

and it can be expressed in terms of Wigner-3j symbols,

$$\mathcal{G}^{\ell L L_1}_{mMM_1} = \left(\frac{(2\ell+1)(2L+1)(2L_1+1)}{4\pi}\right)^{\frac{1}{2}} \begin{pmatrix} \ell & L & L_1 \\ 0 & 0 & 0 \end{pmatrix} \times \begin{pmatrix} \ell & L & L_1 \\ m & M & M_1 \end{pmatrix}. \tag{A15}$$

The Wigner 3j symbols obey an orthogonality relation

$$\sum_{mM} \begin{pmatrix} \ell & L & L_1 \\ m & M & M_1 \end{pmatrix} \begin{pmatrix} \ell & L & L_2 \\ m & M & M_2 \end{pmatrix} = \frac{\delta^K_{L_1 L_2} \delta^K_{M_1 M_2} \delta^T(\ell, L, L_1)}{2L_1+1}\,, \tag{A16}$$

where $\delta^T(\ell, L, L_1)$ enforces the triangle relation that is also obeyed by the 3j-symbols. That is, the Gaunt factor is only nonzero when

$$m + M + M_1 = 0\,, \tag{A17}$$

$$|\ell - L| \leqslant L_1 \leqslant \ell + L\,. \tag{A18}$$

Assuming the triangle condition is satisfied, for even $J = \ell + L + L_1$ we have

$$\begin{pmatrix} \ell & L & L_1 \\ 0 & 0 & 0 \end{pmatrix} = (-1)^{\frac{1}{2}J} \left(\frac{(J-2\ell)!(J-2L)!(J-2L_1)!}{(J+1)!}\right)^{\frac{1}{2}} \times \frac{\left(\frac{1}{2}J\right)!}{\left(\frac{1}{2}J-\ell\right)!\left(\frac{1}{2}J-L\right)!\left(\frac{1}{2}J-L_1\right)!}\,, \tag{A19}$$

for odd $J = \ell + L + L_1$, those 3j's vanish when $m = M = M_1 = 0$.

Appendix B: The Laplacian in an expanding universe

We use the SFB decomposition because that correlates radial and angular modes of the same scale. Here we show that the Laplacian in a flat expanding universe takes the form Eq. (38).

The flat Robertson-Walker metric is

$$ds^2 = -dt^2 + a^2\left[dr^2 + r^2 d\theta^2 + r^2\sin^2\theta\, d\phi^2\right], \quad \text{(B1)}$$

where r is the comoving coordinate, and the metric has the non-zero Christoffel symbols

$$\begin{aligned}
&\Gamma^0_{11} = a^2 H\,, && \Gamma^0_{22} = a^2 r^2 H\,, && \Gamma^0_{33} = a^2 r^2\sin^2\theta\, H\,,\\
&\Gamma^1_{01} = \Gamma^1_{10} = H\,, && \Gamma^1_{22} = -r\,, && \Gamma^1_{33} = -r\sin^2\theta\,,\\
&\Gamma^2_{02} = \Gamma^2_{20} = H\,, && \Gamma^2_{12} = \Gamma^2_{21} = \frac{1}{r}\,, && \Gamma^2_{33} = -\cos\theta\sin\theta\,,\\
&\Gamma^3_{03} = \Gamma^3_{30} = H\,, && \Gamma^3_{13} = \Gamma^3_{31} = \frac{1}{r}\,, && \Gamma^3_{23} = \Gamma^3_{32} = \frac{\cos\theta}{\sin\theta}\,.
\end{aligned}$$

Therefore,

$$g^{\mu\nu}\Gamma^0_{\mu\nu} = 3H\,, \quad \text{(B2)}$$

$$g^{\mu\nu}\Gamma^1_{\mu\nu} = -2\,a^{-2}\,r^{-1}\,, \quad \text{(B3)}$$

$$g^{\mu\nu}\Gamma^2_{\mu\nu} = -a^{-2}\,r^{-2}\,\frac{\cos\theta}{\sin\theta}\,, \quad \text{(B4)}$$

$$g^{\mu\nu}\Gamma^3_{\mu\nu} = 0\,. \quad \text{(B5)}$$

The d'Alembertian operator for a scalar f is

$$\begin{aligned}
\Box f &= g^{\mu\nu}\, f_{;\mu\nu}\\
&= g^{\mu\nu}\left(\partial_\mu\partial_\nu - \Gamma^\sigma_{\mu\nu}\partial_\sigma\right) f\\
&= \Big[-\partial_0^2 + a^{-2}\,\partial_1^2 + a^{-2}r^{-2}\,\partial_2^2 + a^{-2}r^{-2}\sin^{-2}\theta\,\partial_3^2\\
&\quad - 3H\,\partial_0 + 2\,a^{-2}r^{-1}\,\partial_1 + a^{-2}r^{-2}\,\frac{\cos\theta}{\sin\theta}\,\partial_2\Big] f\\
&= \Big[-\partial_0^2 - 3H\,\partial_0 + a^{-2}\Big(\partial_1^2 + r^{-2}\,\partial_2^2 + r^{-2}\sin^{-2}\theta\,\partial_3^2\\
&\quad + 2\,r^{-1}\,\partial_1 + r^{-2}\,\frac{\cos\theta}{\sin\theta}\,\partial_2\Big)\Big] f\,. \qquad \text{(B6)}
\end{aligned}$$

Identifying the term in parentheses as given by Eq. (38), we get

$$\Box f = \left[-\partial_0^2 - 3H\,\partial_0 + a^{-2}\nabla^2\right] f \quad \text{(B7)}$$

in a flat expanding universe. We can also write Eq. (B7) as

$$\Box f = \left[-a^{-3}\partial_t\left(a^3\,\partial_t\right) + a^{-2}\nabla^2\right] f\,. \quad \text{(B8)}$$

The eigenfunctions to the d'Alembertian are, therefore, separable. If we write an eigenfunction

$$f(t, r, \hat{\boldsymbol{r}}) = p(t)\, g(r)\, h(\hat{\boldsymbol{r}}) \quad \text{(B9)}$$

with

$$\nabla^2[g(r)\, h(\hat{\boldsymbol{r}})] = -k^2\, g(r)\, h(\hat{\boldsymbol{r}})\,, \quad \text{(B10)}$$

then

$$0 = a^{-3}\,\partial_t\left(a^3\,\partial_t p\right) + \left[a^{-2}k^2 - \lambda^2\right] p\,, \quad \text{(B11)}$$

where $-\lambda^2$ is the eigenvalue of the d'Alembertian. Since ar is the angular diameter distance and r is the comoving distance (also comoving angular diameter distance), we can call k a comoving mode.

Appendix C: Radial spherical Fourier-Bessel modes with potential boundary conditions

In this appendix we derive the radial basis functions of the Laplacian with potential boundary conditions at $r_{\rm min}$ and $r_{\rm max}$.

We first isolate the radial part of Eq. (38). Writing

$$f(\boldsymbol{r}) = g(r)\, h(\hat{\boldsymbol{r}})\,, \quad \text{(C1)}$$

we require

$$-k^2 gh = \frac{h}{r^2}\,\frac{\partial}{\partial r}\left(r^2\,\frac{\partial g}{\partial r}\right) + g\,\nabla^2 h\,. \quad \text{(C2)}$$

Given the spherical harmonic solution for the angular term h,

$$\nabla^2 h = -\frac{\ell(\ell+1)}{r^2}\,h\,, \quad \text{(C3)}$$

we get

$$0 = \frac{\mathrm{d}}{\mathrm{d}r}\left(r^2\,\frac{\mathrm{d}g_\ell(kr)}{\mathrm{d}r}\right) + \left[(kr)^2 - \ell(\ell+1)\right] g_\ell(kr)\,, \quad \text{(C4)}$$

where we now added that the function g depends on ℓ. Our first aim is to derive the discrete spectrum of k modes for a given ℓ. We then use that to derive the form of the g_ℓ. Following Fisher *et al.* (1995), we demand that the orthogonality relation Eq. (42) is satisfied. However, we modify the approach in Fisher *et al.* (1995) to integrate from $r_{\rm min}$ to $r_{\rm max}$. Eq. (C4) multiplied by $g_\ell(kr)$ then yields

$$\begin{aligned}
&\int_{r_{\rm min}}^{r_{\rm max}} \mathrm{d}r\,\frac{\mathrm{d}}{\mathrm{d}r}\left(r^2\,\frac{\mathrm{d}g_\ell(kr)}{\mathrm{d}r}\right) g_\ell(k'r)\\
&= \int_{r_{\rm min}}^{r_{\rm max}} \mathrm{d}r\left[\ell(\ell+1) - (kr)^2\right] g_\ell(kr)\, g_\ell(k'r)\,. \qquad \text{(C5)}
\end{aligned}$$

Subtract from this equation the same equation with k and k' interchanged,

$$\begin{aligned}
&\left[k'^2 - k^2\right]\int_{r_{\rm min}}^{r_{\rm max}} \mathrm{d}r\, r^2\, g_\ell(kr)\, g_\ell(k'r)\\
&= \int_{r_{\rm min}}^{r_{\rm max}} \mathrm{d}r\left\{\frac{\mathrm{d}}{\mathrm{d}r}\left(r^2\,\frac{\mathrm{d}g_\ell(kr)}{\mathrm{d}r}\right) g_\ell(k'r)\right.\\
&\quad \left. - \frac{\mathrm{d}}{\mathrm{d}r}\left(r^2\,\frac{\mathrm{d}g_\ell(k'r)}{\mathrm{d}r}\right) g_\ell(kr)\right\}. \qquad \text{(C6)}
\end{aligned}$$

Partial integration with the terms on the right hand side (r.h.s.) yields

$$\begin{aligned}
&\int \mathrm{d}r\,\frac{\mathrm{d}}{\mathrm{d}r}\left(kr^2 g'_\ell(kr)\right) g_\ell(k'r)\\
&= kr^2 g'_\ell(kr) g_\ell(k'r)\Big|_{r_{\rm min}}^{r_{\rm max}} - kk'\int \mathrm{d}r\, r^2\, g'_\ell(kr) g'_\ell(k'r)\,. \qquad \text{(C7)}
\end{aligned}$$

Then, Eq. (C6) becomes

$$\left[k'^2 - k^2\right] \int_{r_{\min}}^{r_{\max}} \mathrm{d}r\, r^2\, g_\ell(kr)\, g_\ell(k'r) = kr^2 g'_\ell(kr) g_\ell(k'r)\Big|_{r_{\min}}^{r_{\max}} - k' r^2 g'_\ell(k'r) g_\ell(kr)\Big|_{r_{\min}}^{r_{\max}} . \tag{C8}$$

The r.h.s. will vanish for any k whenever

$$0 = A k r_{\max}^2 g'_\ell(k r_{\max}) - B r_{\max}^2 g_\ell(k r_{\max}) - a k r_{\min}^2 g'_\ell(k r_{\min}) + b r_{\min}^2 g_\ell(k r_{\min}) . \tag{C9}$$

for any constants a, b, A, and B.

To choose a, b, A, and B, we note that the representable field $\delta(\boldsymbol{r})$ is written as a sum of the solutions to Eq. (C4) inside the SFB volume, and we have some freedom to choose the desired behavior outside of it. Since the field inside the SFB volume satisfies the Poisson equation, it is natural to have it satisfy Laplace's equation[9] outside it, and demand that the solution is continuous and smooth at the boundaries. That is,

$$\delta(\boldsymbol{r}) = \begin{cases} \sum_{\ell m} \left[a_{\ell m} \left(\frac{r}{r_{\min}}\right)^\ell + b_{\ell m} \left(\frac{r_{\min}}{r}\right)^{\ell+1} \right] Y_{\ell m}(\hat{\boldsymbol{r}}) , & \text{for } r < r_{\min} , \\ \sum_{n\ell m} \left[c_{n\ell}\, j_\ell(k_{n\ell}\, r) + d_{n\ell}\, y_\ell(k_{n\ell}\, r) \right] Y_{\ell m}(\hat{\boldsymbol{r}})\, \delta_{n\ell m} , & \text{for } r_{\min} \leqslant r \leqslant r_{\max} , \\ \sum_{\ell m} \left[A_{\ell m} \left(\frac{r}{r_{\max}}\right)^\ell + B_{\ell m} \left(\frac{r_{\max}}{r}\right)^{\ell+1} \right] Y_{\ell m}(\hat{\boldsymbol{r}}) , & \text{for } r > r_{\max} , \end{cases} \tag{C10}$$

where we defined the constants $a_{\ell m}$, $b_{\ell m}$, $c_{n\ell}$, $d_{n\ell}$, $A_{\ell m}$, and $B_{\ell m}$, and we explicitly wrote

$$g_\ell(kr) = c_{n\ell}\, j_\ell(kr) + d_{n\ell}\, y_\ell(kr) , \tag{C11}$$

and we anticipate that the function g_ℓ will also depend on n. Continuity at the boundaries requires

$$a_{\ell m} + b_{\ell m} = \sum_n g_\ell(k_{n\ell}\, r_{\min})\, \delta_{n\ell m} , \tag{C12}$$

$$A_{\ell m} + B_{\ell m} = \sum_n g_\ell(k_{n\ell}\, r_{\max})\, \delta_{n\ell m} . \tag{C13}$$

Smoothness further requires

$$\ell \frac{a_{\ell m}}{r_{\min}} - (\ell+1) \frac{b_{\ell m}}{r_{\min}} = \sum_n k_{n\ell}\, g'_\ell(k_{n\ell}\, r_{\min})\, \delta_{n\ell m} , \tag{C14}$$

$$\ell \frac{A_{\ell m}}{r_{\max}} - (\ell+1) \frac{B_{\ell m}}{r_{\max}} = \sum_n k_{n\ell}\, g'_\ell(k_{n\ell}\, r_{\max})\, \delta_{n\ell m} , \tag{C15}$$

Now requiring $\delta(\boldsymbol{r})$ to be finite at $r = 0$ and $r = \infty$ sets $b_{\ell m} = A_{\ell m} = 0$, and requiring continuity and smoothness for any $\delta_{n\ell m}$, we get

$$\ell\, g_\ell(k_{n\ell}\, r_{\min}) = k_{n\ell}\, r_{\min}\, g'_\ell(k_{n\ell}\, r_{\min}) , \tag{C16}$$

$$-(\ell+1)\, g_\ell(k_{n\ell}\, r_{\max}) = k_{n\ell}\, r_{\max}\, g'_\ell(k_{n\ell}\, r_{\max}) . \tag{C17}$$

These choices lead to $a = 1$, $b = \ell/r_{\min}$, $A = 1$, and $B = -(\ell+1)/r_{\max}$ in Eq. (C9), which shows that the conditions Eqs. (C16) and (C17) on $k_{n\ell}$ lead to an orthogonality relation for the g_ℓ.

Both j_ℓ and y_ℓ satisfy the two recurrence relations

$$j'_\ell(kr) = -j_{\ell+1}(kr) + \frac{\ell}{kr}\, j_\ell(kr) , \tag{C18}$$

$$j'_\ell(kr) = j_{\ell-1}(kr) - \frac{\ell+1}{kr}\, j_\ell(kr) . \tag{C19}$$

Then, Eqs. (C16) and (C17) simplify to

$$c_{n\ell}\, j_{\ell+1}(k_{n\ell}\, r_{\min}) + d_{n\ell}\, y_{\ell+1}(k_{n\ell}\, r_{\min}) = 0 , \tag{C20}$$

$$c_{n\ell}\, j_{\ell-1}(k_{n\ell}\, r_{\max}) + d_{n\ell}\, y_{\ell-1}(k_{n\ell}\, r_{\max}) = 0 . \tag{C21}$$

The normalization of g_ℓ is obtained by dividing Eq. (C8) by $k'^2 - k^2$, and taking the limit $k' \to k = k_{n\ell}$,

$$1 = \int_{r_{\min}}^{r_{\max}} \mathrm{d}r\, r^2\, g_\ell^2(kr) = \lim_{k' \to k} \frac{kr^2 g'_\ell(kr) g_\ell(k'r)\big|_{r_{\min}}^{r_{\max}} - k' r^2 g'_\ell(k'r) g_\ell(kr)\big|_{r_{\min}}^{r_{\max}}}{k'^2 - k^2} . \tag{C22}$$

When $kr = k_{n\ell} r_{\min}$ as in Eq. (C16),

$$kr\, g'_\ell(kr) g_\ell(k'r) - k' r\, g'_\ell(k'r) g_\ell(kr) = k' r\, g_\ell(kr) \left[c_{n\ell}\, j_{\ell+1}(k'r) + d_{n\ell}\, y_{\ell+1}(k'r) \right] , \tag{C23}$$

and when $kr = k_{n\ell} r_{\max}$ as in Eq. (C17),

$$kr\, g'_\ell(kr) g_\ell(k'r) - k' r\, g'_\ell(k'r) g_\ell(kr) = -k' r\, g_\ell(kr) \left[c_{n\ell}\, j_{\ell-1}(k'r) + d_{n\ell}\, y_{\ell-1}(k'r) \right] . \tag{C24}$$

[9] Laplace's equation is Poisson's equation without a source term.

The terms in brackets vanish in the limit $k' \to k = k_{n\ell}$ as per Eqs. (C20) and (C21). That is, we need limits

$$\lim_{q'\to q} \frac{c_{n\ell}\, j_{\ell+1}(q') + d_{n\ell}\, y_{\ell+1}(q')}{q'^2 - q^2} = \frac{g_\ell(q)}{2q}\,, \tag{C25}$$

$$\lim_{q'\to q} \frac{c_{n\ell}\, j_{\ell-1}(q') + d_{n\ell}\, y_{\ell-1}(q')}{q'^2 - q^2} = -\frac{g_\ell(q)}{2q}\,, \tag{C26}$$

for $q = kr_{\min}$ and $q = kr_{\max}$, respectively. Then, Eq. (C22) becomes

$$1 = \frac{r_{\max}^3}{2}\, g_\ell^2(k_{n\ell}\, r_{\max}) - \frac{r_{\min}^3}{2}\, g_\ell^2(k_{n\ell}\, r_{\min})\,. \tag{C27}$$

Choosing $k_{n\ell}$, $c_{n\ell}$, and $d_{n\ell}$ that satisfy Eqs. (C20), (C21) and (C27) guarantees the orthonormality of the g_ℓ,

$$\int_{r_{\min}}^{r_{\max}} \mathrm{d}r\, r^2\, g_\ell(k_{n\ell}\, r)\, g_\ell(k_{n'\ell}\, r) = \delta^K_{nn'}\,. \tag{C28}$$

Note that the condition $\ell = \ell'$ is *not* enforced by the g_ℓ. Instead, $\ell = \ell'$ comes from the spherical harmonics, i.e., Eq. (A7).

1. Phase factor

We are free to introduce a phase factor for the $g_{n\ell}(r)$, and we choose it so that the sign of $g_{n\ell}(r_{\min})$ alternates with n, but stays constant with ℓ,

$$g_{n\ell}(r) = (-1)^{\left[1-\mathrm{floor}\left(\frac{1}{\ell+1}\right)\right]\left[1-\mathrm{floor}\left(\frac{1}{n}\right)\right]}\, \tilde{g}_{n\ell}(r)\,, \tag{C29}$$

where the tilde indicates that we have not included the phase factor. This flips the sign unless either $\ell \neq 0$ or $n \neq 1$. Thus, the basis functions in Fig. 4 are obtained.

2. Numerical concerns

To calculate $k_{n\ell}$, solve each of Eqs. (C20) and (C21) for the ratio $d_{n\ell}/c_{n\ell}$, and set them equal to get

$$\begin{aligned} 0 = {} & j_{\ell-1}(k_{n\ell}\, r_{\max})\, y_{\ell+1}(k_{n\ell}\, r_{\min}) \\ & - y_{\ell-1}(k_{n\ell}\, r_{\max})\, j_{\ell+1}(k_{n\ell}\, r_{\min})\,. \end{aligned} \tag{C30}$$

Examples for the resulting zeros and the first few basis functions are shown in Fig. 4. The ratio $d_{n\ell}/c_{n\ell}$ then follows from Eq. (C20) or Eq. (C21). Finally, the overall normalization is fixed by Eq. (C27) up to a sign.

When $r_{\max}$ is large and $r_{\min}$ is small, the $k_{n\ell}$ may need to be computed using arbitrary precision floats, and the $g_{n\ell}$ may need to be calculated with arbitrary precision as well. Caching the result in double precision should then provide for sufficient speed for the actual transform.

Appendix D: Covariance matrix simplification

In this appendix we simplify the covariance matrix Eq. (112). For simplicity we ignore the local average effect. We explicitly treat the shot noise Eq. (79) because it is inhomogeneous and anisotropic. We get

$$\left\langle \delta^{W,A}_{NLM}\, \delta^{W,A,*}_{N'L'M'} \right\rangle = \sum_{n_1\ell_1m_1} W^{n_1\ell_1m_1}_{NLM} \sum_{n_2\ell_2m_2} W^{n_2\ell_2m_2,*}_{N'L'M'} \left[\delta^K_{\ell_1\ell_2}\delta^K_{m_1m_2}\, C_{\ell_1n_1n_2} + \frac{1}{\bar{n}} \left(W^{-1}\right)^{n_2\ell_2m_2}_{n_1\ell_1m_1} \right] \tag{D1}$$

$$= \sum_{\ell_1n_1n_2} C_{\ell_1n_1n_2} \sum_{m_1} W^{n_1\ell_1m_1}_{NLM} W^{N'L'M'}_{n_2\ell_1m_1} + \frac{1}{\bar{n}} W^{N'L'M'}_{NLM}\,, \tag{D2}$$

where we used Eq. (53). Similarly, when neither density contrast has the complex conjugate attached,

$$\left\langle \delta^{W,A}_{NLM}\, \delta^{W,A}_{N'L'M'} \right\rangle = (-1)^{M'} \sum_{\ell_1n_1n_2} C_{\ell_1n_1n_2} \sum_{m_1} W^{n_1\ell_1m_1}_{NLM} W^{N'L',-M'}_{n_2\ell_1m_1} + \frac{(-1)^{M'}}{\bar{n}} W^{N'L',-M'}_{NLM}\,, \tag{D3}$$

where we used Eq. (A12). Therefore, both terms in Eq. (112) are of the form

$$\begin{aligned} & \frac{1}{(2\ell+1)(2L+1)} \sum_{mM} \left\langle \delta^{W,A}_{n\ell m} \delta^{W,A,*}_{NLM} \right\rangle \left\langle \delta^{W,A}_{n'\ell m} \delta^{W,A,*}_{N'LM} \right\rangle \\ & = \frac{1}{(2\ell+1)(2L+1)} \sum_{mM} \left[\sum_{\ell_1n_1n_2} C_{\ell_1n_1n_2} \sum_{m_1} W^{n_1\ell_1m_1}_{n\ell m} W^{NLM}_{n_2\ell_1m_1} + \frac{1}{\bar{n}} W^{NLM}_{n\ell m} \right] \\ & \quad \times \left[\sum_{\ell_3n_3n_4} C_{\ell_3n_3n_4} \sum_{m_3} W^{n_3\ell_3m_3,*}_{n'\ell m} W^{N'LM,*}_{n_4\ell_3m_3} + \frac{1}{\bar{n}} W^{N'LM,*}_{n'\ell m} \right] \end{aligned} \tag{D4}$$

$$= \frac{1}{(2\ell+1)(2L+1)} \sum_{mM} \Bigg[\sum_{\ell_1 n_1 n_2} C_{\ell_1 n_1 n_2} \sum_{m_1} W^{n_1 \ell_1 m_1}_{n \ell m} W^{NLM}_{n_2 \ell_1 m_1} \sum_{\ell_3 n_3 n_4} C_{\ell_3 n_3 n_4} \sum_{m_3} W^{n_3 \ell_3 m_3,*}_{n' \ell m} W^{N'LM,*}_{n_4 \ell_3 m_3}$$

$$+ \frac{1}{\bar{n}} W^{NLM}_{n\ell m} \frac{1}{\bar{n}} W^{N'LM,*}_{n'\ell m} + \frac{1}{\bar{n}} W^{N'LM,*}_{n'\ell m} \sum_{\ell_1 n_1 n_2} C_{\ell_1 n_1 n_2} \sum_{m_1} W^{n_1 \ell_1 m_1}_{n\ell m} W^{NLM}_{n_2 \ell_1 m_1} + \big\langle n \leftrightarrow n', N \leftrightarrow N' \big\rangle^* \Bigg] \tag{D5}$$

$$= A_1{}^{LNN'}_{\ell n n'} + A_2{}^{LNN'}_{\ell n n'} + A_2{}^{LN'N}_{\ell n' n} + A_3{}^{LNN'}_{\ell n n'} \,. \tag{D6}$$

Using Eq. (53), we get

$$A_1{}^{LNN'}_{\ell n n'} = \frac{1}{(2\ell+1)(2L+1)} \sum_{\ell_1 n_1 n_2} C_{\ell_1 n_1 n_2} \sum_{\ell_3 n_3 n_4} C_{\ell_3 n_3 n_4} W_4 \begin{pmatrix} \ell_1 & L & \ell_3 & \ell \\ n_1 & N & n_4 & n' \\ n_2 & N' & n_3 & n \end{pmatrix}, \tag{D7}$$

and

$$A_2{}^{LNN'}_{\ell n n'} = \frac{1}{\bar{n}} \frac{1}{(2\ell+1)(2L+1)} \sum_{\ell_1 n_1 n_2} C_{\ell_1 n_1 n_2} W_3 \begin{pmatrix} \ell_1 & L & \ell \\ n_1 & N & n' \\ n_2 & N' & n \end{pmatrix}, \tag{D8}$$

and

$$A_3{}^{LNN'}_{\ell n n'} = \frac{1}{\bar{n}^2} \frac{1}{(2\ell+1)(2L+1)} W_2 \begin{pmatrix} L & \ell \\ N & n' \\ N' & n \end{pmatrix} = \frac{1}{\bar{n}^2} \frac{1}{2\ell+1} \mathcal{M}^{LNN'}_{\ell n n'} \,. \tag{D9}$$

The W_k symbols are defined in Eq. (E1) and discussed in Appendix E. Then Eq. (112) becomes

$$V^W{}^{LNN'}_{\ell n n'} = A_1{}^{LNN'}_{\ell n n'} + A_2{}^{LNN'}_{\ell n n'} + A_2{}^{LN'N}_{\ell n' n} + A_3{}^{LNN'}_{\ell n n'} + \big\langle N \leftrightarrow N' \big\rangle . \tag{D10}$$

The A_1 term dominates if the power spectrum is much larger than the shot noise, and A_3 dominates if shot noise is larger.

Appendix E: Chains of window functions

Throughout the paper, we find that traces of density-contrast window coupling matrices W appear with summations over the azimuthal modes m. That is, we find tensors W_k of the form

$$W_k \begin{pmatrix} \ell_1 & \ell_2 & \dots & \ell_k \\ n_1 & n_2 & \dots & n_k \\ n'_1 & n'_2 & \dots & n'_k \end{pmatrix} = \sum_{m_1 m_2 \dots m_k} W^{n_1 \ell_1 m_1}_{n'_k \ell_k m_k} W^{n_2 \ell_2 m_2}_{n'_1 \ell_1 m_1} \cdots W^{n_k \ell_k m_k}_{n'_{k-1} \ell_{k-1} m_{k-1}} \,. \tag{E1}$$

This starts with a single window function Eq. (80) ($k = 1$) for shot noise, two window functions Eqs. (67) and (D9) ($k = 2$) for the pseudo power spectrum mixing matrix and shot noise covariance, three window functions Eqs. (107) and (D8) for part of the local average effect and covariance calculations, four window functions Eq. (D7). If we were to include the local average effect in the covariance, then $k = 5$ and $k = 6$ would also occur.

The W_k are real, which is trivially shown by substituting each window with its definition Eq. (51) and using Eq. (A11). Also, cyclical permutations of the argument columns leave W_k invariant, and anticyclical permutations leave it invariant if all n_i and n'_i are switched as well. That is,

$$W_k \begin{pmatrix} \ell_1 & \ell_2 & \dots & \ell_k \\ n_1 & n_2 & \dots & n_k \\ n'_1 & n'_2 & \dots & n'_k \end{pmatrix} = W_k \begin{pmatrix} \ell_k & \ell_1 & \dots & \ell_{k-1} \\ n_k & n_1 & \dots & n_{k-1} \\ n'_k & n'_1 & \dots & n'_{k-1} \end{pmatrix} = W_k \begin{pmatrix} \ell_k & \ell_{k-1} & \dots & \ell_1 \\ n'_k & n'_{k-1} & \dots & n'_1 \\ n_k & n_{k-1} & \dots & n_1 \end{pmatrix}. \tag{E2}$$

The first equality trivially follows from the definition Eq. (E1), and the second from applying Eq. (53) to all the windows.

1. Evaluation for separable window function

For a separable window $W(\boldsymbol{r}) = \phi(r)\, W(\hat{\boldsymbol{r}})$, Eq. (56) becomes

$$W^{n\ell m}_{n'\ell' m'} = I^{n\ell}_{n'\ell'}\, W^{\ell m}_{\ell' m'}\,, \tag{E3}$$

where

$$I^{n\ell}_{n'\ell'} = \int_{r_{\rm min}}^{r_{\rm max}} {\rm d}r\, r^2\, g_{n'\ell'}(r)\, g_{n\ell}(r)\, \phi(r)\,, \tag{E4}$$

$$W^{\ell m}_{\ell' m'} = (-1)^{m'} \sum_{LM} \mathcal{G}^{\ell'\ell L}_{-m',m,M}\, W_{LM}\,, \tag{E5}$$

where W_{LM} was defined in Eq. (71). Thus, Eq. (E1) is

$$W_k \begin{pmatrix} \ell_1 & \ell_2 & \dots & \ell_k \\ n_1 & n_2 & \dots & n_k \\ n'_1 & n'_2 & \dots & n'_k \end{pmatrix} = I^{n_1\ell_1}_{n'_k\ell_k}\, I^{n_2\ell_2}_{n'_1\ell_1} \cdots I^{n_k\ell_k}_{n'_{k-1}\ell_{k-1}} \sum_{m_1 m_2 \dots m_k} W^{\ell_1 m_1}_{\ell_k m_k}\, W^{\ell_2 m_2}_{\ell_1 m_1} \cdots W^{\ell_k m_k}_{\ell_{k-1} m_{k-1}}\,. \tag{E6}$$

Eq. (E6) contains $\mathcal{O}\big(\ell^k\big)$ terms.